

Oxygen Vacancy Formation and Water Adsorption on Reduced AnO_2 {111}, {110} and {100} Surfaces (An = U, Pu); A Computational Study

Joseph P. W. Wellington,¹ Bengt E. Tegner,² Jonathan Collard,² Andrew Kerridge³
and Nikolas Kaltsoyannis*²

¹ Department of Chemistry, University College London, 20 Gordon Street, London
WC1H 0AJ, UK

² School of Chemistry, The University of Manchester, Oxford Road, Manchester, M13
9PL, UK

³ Department of Chemistry, The University of Lancaster, Lancaster, LA1 4YB, UK

*Correspondence: nikolas.kaltsoyannis@manchester.ac.uk

Abstract

The substoichiometric {111}, {110} and {100} surfaces of UO_2 and PuO_2 are studied computationally using two distinct yet related approaches based on density functional theory; the periodic electrostatic embedded cluster method (PEECM) and Hubbard-corrected periodic boundary condition DFT. First and second layer oxygen vacancy formation energies and geometries are presented and discussed; the energies are found to be substantially larger for UO_2 vs PuO_2 , a result traced to the substantially more positive An(IV)/An(III) reduction potential for Pu, and hence relative ease of Pu(III) formation. For {110} and {100}, the significantly more stable dissociative water adsorption seen previously for stoichiometric surfaces [*J. Nucl. Mater.* **2016**, 482, 124–134; *J. Phys. Chem. C* **2017**, 121, 1675-1682] is also found for the defect surfaces. By contrast, vacancy creation substantially changes the most stable mode of water adsorption on the {111} surface, such that the almost degenerate molecular and dissociative adsorptions on the pristine surface are replaced by a strong preference for dissociative adsorption on the substoichiometric surface. The implications of this result for the formation of H_2 are discussed. The generally very good agreement between the data from the embedded cluster and periodic DFT approaches provides additional confidence in the reliability of the results and conclusions.

Introduction

The reprocessing of UO_2 -based spent nuclear fuel in the UK has led to the accumulation, over several decades, of significant quantities of highly radioactive PuO_2 . Indeed, the UK holds about half the world's civil inventory of PuO_2 (c. 126 tonnes Pu), stored as a powder in stainless steel containers, while the government decides its eventual fate. Options include long term storage in a geological disposal facility, or reuse in mixed oxide fuel, but for the time being the material is kept in the steel containers pending a final decision. However, some containers have distorted, leading to the hypothesis that gas build up has occurred, possibly as a result of water vapor desorbing from the PuO_2 , hydrogen gas from the radiolysis of adsorbed water, or the reaction of such water with the PuO_2 . It is essential that we fully understand the causes of the container distortions and, as experimental measurements are severely limited by the intense radioactivity of Pu, we are exploring these possibilities computationally, recently reporting the first results of our studies; the geometries and energetics of water adsorption on the low Miller index $\{111\}$, $\{110\}$ and $\{100\}$ surfaces of UO_2 and PuO_2 .^{1,2}

Our previous work involved only stoichiometric surfaces. However, most solid state materials have defects present and at surfaces, dependent on their type and concentration, defects can have significant effects on the type of adsorption that can occur, and of the energetics of the processes. We have therefore moved on to study defect surfaces, and report the first results of this extension in this contribution. While there are many different types of defects that can occur in solid state systems, in this study we focus on oxygen vacancies, their formation energies and the adsorption of water on or near them. We again concentrate on the $\{111\}$, $\{110\}$ and $\{100\}$ surfaces of UO_2 and PuO_2 .

In our previous studies we have employed both periodic, plane-wave density functional theory (DFT)² and also DFT within an embedded cluster approach,¹ arguing that the fullest possible computational description of water adsorption should be furnished by a combination of two different, yet related modelling techniques. It has been very reassuring to see that these quite different formalisms yield very similar results. In this contribution we bring our two approaches together for the first time, and make extensive comparisons between them throughout. We organize the

paper as follows: we start with a brief description of the two computational methodologies used, survey the previous literature and then present vacancy formation energies. We then discuss water adsorption geometries and energies, comparing molecular and dissociative adsorption on or near an oxygen vacancy. Throughout, we compare our data with previous theoretical and, where possible, experimental results.

Computational Details

Periodic calculations

All our periodic calculations were performed using VASP 5.4.1,³⁻⁶ a plane-wave DFT code using Projector-Augmented Wave (PAW)-pseudopotentials^{7,8} to describe the ions and employing Monkhorst-Pack (MP)⁹ grids for the k-space integration. All calculations used a plane wave cut-off of 650 eV and a minimum MP-grid of 5×5×1 k-points for the Brillouin zone sampling for the surface simulations and 11×11×11 for the bulk calculations. The generalized gradient approximation of Perdew, Burke, and Ernzerhof (PBE)¹⁰ with a Hubbard U correction for the 5f electrons,^{11,12} was used for the exchange-correlation energy. An effective U value $U_{eff} = 4.0$ eV was used for both uranium and plutonium, as per our previous calculations.²

The AnO₂ surfaces are constructed using repeating slabs of 24 AnO₂ units arranged in six layers, each with 18 Å of vacuum between each slab. The atom positions are allowed to relax until the net inter-atomic forces are below 0.001 eV/Å. We use 1-k co-linear magnetic ordering with a net magnetic moment of zero, allowing us to treat the total system as anti-ferromagnetic and thereby reach the correct ground state.^{13,14} We neglect spin-orbit coupling, as earlier results by Rák and co-workers¹⁵ indicate that spin-orbit coupling only has a very small effect on the surface stability. Defects and adsorbates are introduced on both sides of the slab to minimize dipole effects. All the periodic images were made using VESTA.¹⁶

The vacancy formation energy was calculated using the following expression

$$E_{\text{vacancy}} = \frac{1}{2}(E_{\text{red,slab}} - (E_{\text{slab}} - E_{\text{O}_2})) \quad (1)$$

Where $E_{\text{red,slab}}$ is the energy of the relaxed reduced slab, E_{slab} is the energy of the relaxed stoichiometric slab of the same type and E_{O_2} is the energy of a single oxygen molecule in a box with a 20 Å side. The factor of 1/2 is due to the reduced slab having one vacancy per side.

Embedded cluster calculations

All embedded cluster calculations were performed with the TURBOMOLE program.¹⁷ We have previously shown¹ that the PBE¹⁸ (hybrid-GGA) exchange-correlation functional performs well in this context, and have used it to produce all of the data reported here.

The self-consistent field convergence was set to 1×10^{-6} a.u. whilst geometry optimizations were performed with convergence criteria of 1×10^{-6} a.u. for the total energy and 1×10^{-3} a.u. for the maximum norm of the cartesian energy gradient.

As described in reference¹, for geometry optimisations, the def-SV(P) basis sets^{19,20} contained in the TURBOMOLE library were used for all oxygen atoms and actinides that used a small core pseudopotential (PP) (see below), and the double-zeta MWB-AVDZ²¹ basis set was used for actinide atoms using a large core PP. This combination is noted from now on as the SV(P) basis set. Single point calculations were performed, at geometries obtained with the SV(P) basis set, with the larger def-QZVP^{20,22} and MWB-AVQZ²¹ basis sets, used with the corresponding small and large core PPs, noted now as the QZVP basis set. PPs were used for the actinide ions in the quantum mechanically treated cluster; small-core (60 electron) def-PPs from the TURBOMOLE library^{23,24} or, where stated, large-core PPs incorporating the 5f electrons,²¹ corresponding to 80 or 82 electron cores for U and Pu respectively - these are electrons with principal quantum number 5 or lower. These 5f-in-core PPs have been parameterized specifically for tetravalent states. When the 5f-in-core PPs are used the clusters are written as $\text{An}_x\text{An}_y\text{O}_{2(x+y)}$ where x refers to the number of

actinide ions with explicit 5f electrons and y to the number of actinide ions described by 5f-in-core PPs.

Dispersion corrections have been included with the Grimme D3 parameters.²⁵

All calculations were performed using the periodic electrostatic embedded cluster method (PEECM).²⁶ In this approach, the system is split into three regions; an inner explicit cluster region, which is treated quantum mechanically as described above; the outer embedding region, consisting of point charges; and an intermediate region, consisting of negative point charges and PPs. The infinite outer embedding region recreates the Madelung potential of the bulk system: formal charges were used for the ions in this region, +4 for actinide ions and -2 for oxygen ions. The PPs used in the intermediate region were the Ce CRENB L PPs,²⁷ employed in order to avoid overpolarization of the electron density in the explicit cluster, whilst -2 charges again represent the oxygen ions. The Ce CRENB L PP, which corresponds to a +4 charge when used without any basis functions, was used since no actinide PPs corresponding to a +4 charge are available. The 8-coordinate Ce(IV) ionic radius, 0.97 Å, is very similar to that of U(IV) and Pu(IV), 1.00 Å and 0.96 Å respectively.²⁸

As lattice parameters cannot be optimized within the PEECM, experimental lattice parameters were used, $a = 5.470$ and 5.398 Å for UO_2 , and PuO_2 respectively, which are all in the space group $\text{Fm}\bar{3}m$.

By contrast to our periodic DFT calculations, in our PEECM model the metal ions are coupled ferromagnetically, with 2 or 4 unpaired electrons per actinide ion for UO_2 and PuO_2 respectively. I.e. we converge on the high spin ground state within the spin unrestricted Kohn Sham formalism – by no means straightforward for systems with so many unpaired 5f electrons. This is logical, as although bulk AnO_2 are known to be antiferromagnetic, the local magnetic ordering in a small molecular cluster of c. 20 AnO_2 units is not necessarily so, and the high-spin state is the one that can be most reliably modelled using DFT in a molecular context. We note that the difference in energy between ferromagnetic and antiferromagnetic ordering in actinide oxides has been seen in previous theoretical studies to be very small, in the order of tens of meV with a hybrid functional.^{29–31} Furthermore, the similarities in the results of our

previous periodic and embedded cluster DFT studies suggest that the local magnetic ordering has little impact on water adsorption.

Initially, oxygen vacancy formation energies were calculated with the following equation:

$$E_{\text{form}} = E_{\text{surf+O}_{\text{vac}}} - E_{\text{surf}} + \frac{1}{2} E_{\text{O}_2} \quad (2)$$

where $E_{\text{surf+O}_{\text{vac}}}$ is the energy of the cluster with an oxygen vacancy, E_{surf} the energy of the stoichiometric cluster and E_{O_2} is the energy of the gas phase O_2 molecule. The O_2 molecule in its triplet state is used as a reference state, as opposed to the O atom, as most previous theoretical studies^{32–38} use this reference state. As the dissociation energy of the O_2 molecule is very method dependent (e.g. it is in good agreement with experiment using hybrid functionals, while it is overestimated with GGA functionals) using the O atom as a reference state would cause large variation in the oxygen vacancy formation energy obtained from different DFT methods. Furthermore, using O_2 as a reference is aligned with the approach taken in our periodic DFT calculations.

The two electrons left when a neutral oxygen vacancy is formed are unpaired (with the same spin as the unpaired electrons on the actinide ions) as this was calculated to be more stable than the paired scenario. Hence for a calculation of the $\text{U}_{19}\text{O}_{37}$ cluster, for example, there are 40 unpaired electrons: 38 from the uranium ions, and two from the oxygen vacancy.

Basis set superposition error (BSSE) was accounted for with the counterpoise correction (CP) approach; the stoichiometric surface was taken as the whole system, while a single oxygen atom and the cluster with an oxygen vacancy were taken as the fragments. Thus the BSSE is calculated as:

$$\text{BSSE} = E_{\text{surf+O}_{\text{vac}}+\text{O}}^{\text{surf+O}_{\text{vac}}+\text{O}} - E_{\text{surf+O}_{\text{vac}}}^{\text{surf+O}_{\text{vac}}} + \frac{1}{2} E_{\text{O}_2}^{\text{surf+O}_{\text{vac}}+\text{O}} - \frac{1}{2} E_{\text{O}_2}^{\text{O}_{\text{vac}}} \quad (3)$$

The parts of the system with basis sets included in the calculation are shown in superscript, and the parts of the system included in the electronic structure

calculation are shown in subscript. The BSSE energy was then added to the energy of the stoichiometric surface and the oxygen vacancy formation energy recalculated.

Summary of Previous Literature

Defect chemistry in transition metal or rare earth oxides is often hard to model with DFT; in particular, electron or hole localization due to point defects can be incorrectly described. For example, in TiO_2 the localization or delocalization of electrons due to an oxygen vacancy has been seen to be very method dependent: with a GGA functional electrons are delocalized across the system, whereas with GGA+ U the extent of localization depends on the U value, with an increase in U leading to greater localization. With hybrid functionals both scenarios can be observed, with a preference for electron localization occurring with an increase in the percentage of Hartree-Fock (HF) exchange used.³⁹ Similar results are found with CeO_2 (a material often used as a surrogate for AnO_2 systems in experimental studies) where the localization of electrons left from an oxygen vacancy is again dependent on the method used: GGA functionals lead to delocalization of two electrons across the system,⁴⁰ while increasing values of U in DFT+ U and increasing proportions of HF exchange with hybrid functionals^{26,41,42} leads to greater localization of the electrons on nearby cerium ions. A useful review discussing oxygen defects at the surface of CeO_2 systems is given in reference ⁴³.

(i) Oxygen vacancy formation energies

The properties of defects such as oxygen vacancies are often difficult to study experimentally, particularly for actinide systems. Theoretical studies have therefore been employed, including vacancy formation energies. There have been a number of periodic DFT studies that have investigated oxygen vacancies in UO_2 systems, while PuO_2 , even theoretically, has not been studied in great detail.

Table 1 collates oxygen vacancy formation energies in bulk UO_2 and PuO_2 calculated from different periodic DFT studies. Despite most of these using similar functionals and the DFT+ U method, there is a surprising variation. Two groups have calculated the oxygen vacancy formation energy for both UO_2 and PuO_2 .^{35,38,44,45} Although the values differ substantially between the groups (one set of studies used

GGA and the other GGA+ U), both found that the formation energy is higher in UO_2 than PuO_2 .

Year	Authors	Functional	Oxygen vacancy formation energy	
			UO_2	PuO_2
2005/2006	Freyss ^{35,38}	PBE	6.1	5.3
2006	Iwasawa ³⁶	PBE+ U	4.46	-
2009	Nerikar ³⁷	GGA+ U^*	5.29	-
2010	Dorado ³⁴	PBE+ U	5.67	-
2014	Bo ³²	PBE+ U	6.14	-
2016	Ao ^{44,45}	PW91+ U	6.79	3.76

Table 1. DFT-calculated oxygen vacancy formation energies (eV) for bulk UO_2 or PuO_2 . *GGA functional not specified.

There are very few studies examining point defects – in particular oxygen vacancies – at the surfaces of these systems. Bo *et al.* find, with the PBE+ U method, vacancy formation energies of 5.95 eV and 6.08 eV for the 1st and 2nd layers respectively on the UO_2 {111} surface, and 5.38 eV and 5.59 eV on the UO_2 {110}.³² Sun *et al.* investigated with DFT+ U the effects of oxygen vacancies on surface stability and chemical activity on low index PuO_2 surfaces.⁴⁶ They found oxygen vacancy formation energies, where $\frac{1}{4}$ of the surface layer oxygen atoms were removed, of 2.85 eV on the {111} surface and 1.96 eV on the {110} surface; hence, as for the bulk, these energies are significantly smaller than those found on the UO_2 ³² surfaces. As on the UO_2 {111} surface, there was little difference between the formation energy of a surface or subsurface oxygen vacancy, with the subsurface vacancy only 0.04 eV less stable than the surface vacancy.

Oxygen vacancies in CeO_2 , which is isostructural with AnO_2 and is, as mentioned, often used as a surrogate, have also been studied. Molinari *et al.* found higher oxygen vacancy formation for the {111} surface (2.01 eV) than the {110} (1.29 eV) and, perhaps surprisingly considering the higher surface energy and lower coordination of surface oxygen atoms on the {100} than {110} surface, the {100} surface had a value higher than the {110} surface (1.61 eV).³³

The lower oxygen vacancy formation energies on the {110} than the {111} surface that have been calculated in these MO₂ studies is likely due to the lower coordination number of metal ions on the {110} surface, as well as the higher surface energy of the {110}.

Finally, we note that the PEECM has been used to study oxygen vacancies in bulk and surface CeO₂,²⁶ where their calculated formation energies at the {111} surface were in excellent agreement with a periodic DFT study using the HSE functional,⁴¹ and in good agreement with DFT+*U* studies.^{41,47}

(ii) Effect of oxygen vacancies on water adsorption

The effect of oxygen vacancies on water adsorption has been studied extensively on transition metal and lanthanide oxide surfaces. On the TiO₂ (rutile) {110} surface, despite many experimental and theoretical studies, there is still debate as to whether water adsorbs only molecularly on the stoichiometric surface, or whether it can also adsorb dissociatively.^{48,49} However, when oxygen vacancies are present there is experimental and theoretical agreement that dissociative adsorption occurs.^{50,51} On CeO₂ surfaces, calculations have shown that dissociative water adsorption is favourable vs molecular on the substoichiometric surface.^{33,52} On the substoichiometric Zn (10 $\bar{1}$ 0) surface however, DFT calculations have shown that water does not adsorb dissociatively, but molecularly away from the oxygen vacancy.⁵³ It is clear from these studies that the presence of oxygen vacancies can have a significant impact on water adsorption.

Experiment has shown that water adsorbs reversibly on stoichiometric UO₂,^{54,55} while on sub-stoichiometric UO_{2-x} water adsorption results in the desorption of H₂ from the surface.⁵⁴ The production of H₂ on sub-stoichiometric surfaces implies that the water adsorbs dissociatively; a water molecule adsorbs to the defect site, with the oxygen healing the surface and the hydrogen desorbing as H₂. This would mean the sub-stoichiometric surfaces have a preference for dissociative over molecular adsorption. This is clearly relevant to the storage of PuO₂ as production of H₂ at the surface could contribute to storage container pressurization.

Bo *et al.* investigated the effect of an oxygen vacancy on water adsorption on the {111} and {110} surfaces of UO₂. For molecular adsorption on the sub-stoichiometric

{111} surface they found two stable geometries, while on the sub-stoichiometric {110} surface only one stable geometry was found.¹⁹ For dissociative adsorption, they found one stable geometry on the {111} surface with a hydroxyl filling the oxygen vacancy, and the additional hydrogen adsorbing to an adjacent surface oxygen atom. On the {110} surface two different geometries are found. In both cases the hydroxyl group fills the oxygen vacancy, but in one case the other hydrogen adsorbs to an adjacent oxygen, pointing at the adsorbed hydroxyl, while in the other the hydrogen is adsorbed on a nearby surface oxygen, but points away from the adsorbed hydroxyl. In all cases the presence of an oxygen vacancy increases the adsorption energy.³² On the {111} surface, where molecular and dissociative water adsorption had similar energies in the stoichiometric case, the presence of an oxygen vacancy leads to a preference for dissociative adsorption; the energy of dissociative adsorption increased by 1.52 eV on the substoichiometric vs the stoichiometric surface, but by only 0.33 eV for molecular adsorption. For {110}, there is a preference for dissociative adsorption on the stoichiometric surface. In the substoichiometric case, dissociative adsorption is again more stable than molecular adsorption, although the energy of both types of adsorption increases by a similar amount from the stoichiometric to the substoichiometric surface, dissociative adsorption by 0.84 eV and molecular adsorption by 0.80 eV.

In a separate study Bo *et al.* investigated water adsorption on NpO_2 low index surfaces.⁵⁶ As for the UO_2 surface, the presence of an oxygen vacancy leads to an increase in the adsorption energy, however with only small increases for molecular adsorption – 0.08 eV on the {111} surface and 0.15 eV on the {100} surface (on the {110} surface a water molecule dissociated upon optimisation). There were much greater increases for dissociative adsorption with an oxygen vacancy present; 1.38 eV on the {111} surface, 0.75 eV on the {110} and 0.97 eV on the {100}. It is worth noting that the large increase in the dissociative adsorption energy on the {111} surface leads to a greater adsorption energy on the substoichiometric {111} than {110} surface.

The effect of oxygen vacancies on water adsorption has also been studied on CeO_2 ; an overview of this area is given in Section 4.4 of a review by Paier *et al.*⁴³ On the stoichiometric {111} surface generally small differences are found between molecular

and dissociative adsorption at low coverage (0.01–0.30 eV),^{33,57–59} while water adsorption on the substoichiometric {111} surface strongly favours dissociative adsorption, with increases in the dissociative adsorption energy of up to 1.79 eV.⁵⁹ Molecular adsorption, on the other hand, shows only modest increases in adsorption energy on the reduced surface, and in one case a decrease is seen.⁵⁷

Most studies have focused solely on the {111} CeO₂ surface. Molinari *et al.*, however, also calculated adsorption energies for water on the reduced {110} surface. They calculated an energy of 1.44 eV for dissociative adsorption on the substoichiometric {110} surface (a water molecule dissociates on optimization, therefore they give no value for molecular adsorption), this is an increase of 0.32 eV from the stoichiometric surface.³³ On the substoichiometric surfaces dissociative adsorption restores the coordination number of the nearby metal atoms and it is clear from these studies that an oxygen vacancy causes a stabilisation of dissociative adsorption. This is perhaps unsurprising – molecular adsorption is similar on both the stoichiometric and substoichiometric surfaces, while dissociative adsorption occurs in a completely different way, with a hydroxyl adsorbing onto the oxygen vacancy site on the substoichiometric surface, instead of above a metal ion as on the stoichiometric surface.

Results and Discussion

A Oxygen vacancy geometries

(i) Embedded cluster calculations

Oxygen vacancies were formed in the AnO₂ clusters used for the water adsorption calculations in our previous PEECM study,¹ *i.e.* geometry optimizations of An₅An₁₄O₃₇ for the {111} surface and An₅An₂₀O₄₉ for the {110}, followed by single points on An₁₉O₃₇ for the {111} surface and An₂₅O₄₉ for the {110}. In order to carry out calculations for the {100} surface, a new An₅An₁₆O₄₁ cluster was created. As the true {100} surface is entirely oxygen-terminated (or actinide-terminated, depending on which face is considered) in order to prevent a large dipole moment forming across the surface, half of the oxygen atoms were moved from one side of the surface to the other. Since a dipole could be induced by either an imbalanced cluster or point charge region, this process was applied to both the embedded cluster itself

and the repeating surface cell used to generate the point charges. As a result, the intrinsic dipole moment in the z-direction has been negated at both the quantum-mechanical and electrostatic levels. This solution has previously been used in several papers^{15,56,60} regarding the {100} AnO₂ surfaces and is a widely accepted method of eliminating the inherent dipole of the fluorite structure's {100} surface.

Geometry optimisations were performed such that only atoms in the quantum mechanical (QM) cluster which are coordinated to other atoms in the QM cluster were allowed to relax. An oxygen atom was removed in either the first or second layer; when in the 1st layer, the oxygen atom adjacent to the site of a single molecular water adsorption was chosen. The optimized geometries of the clusters containing oxygen vacancies on the UO₂ {111}, {110} and {100} surfaces are shown in Figure 1, 2 and 3 respectively. Analogous images (not shown) for PuO₂ are very similar.

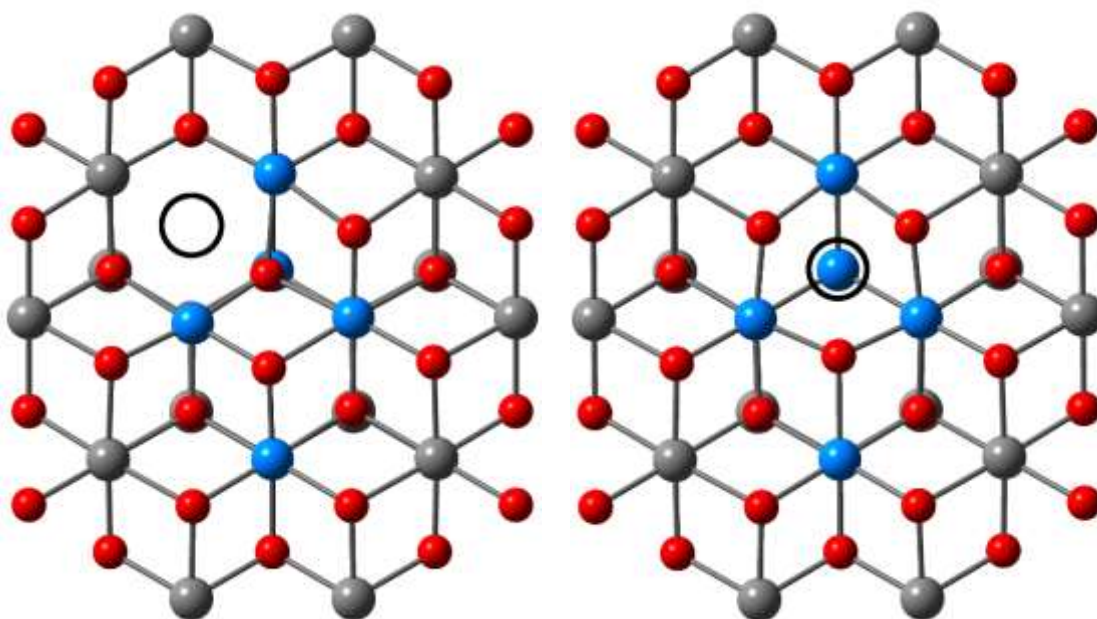


Figure 1 U₅U₁₄O₃₇ cluster containing an oxygen vacancy in the 1st oxygen layer (left) and 2nd layer (right). The cluster is viewed perpendicular to the {111} surface. Oxygen atoms are shown in red and actinide atoms in blue and grey. Grey spheres represent actinide atoms treated with 5f-in-core PPs. The position of the oxygen vacancy is indicated with a black circle. Embedding ions not shown.

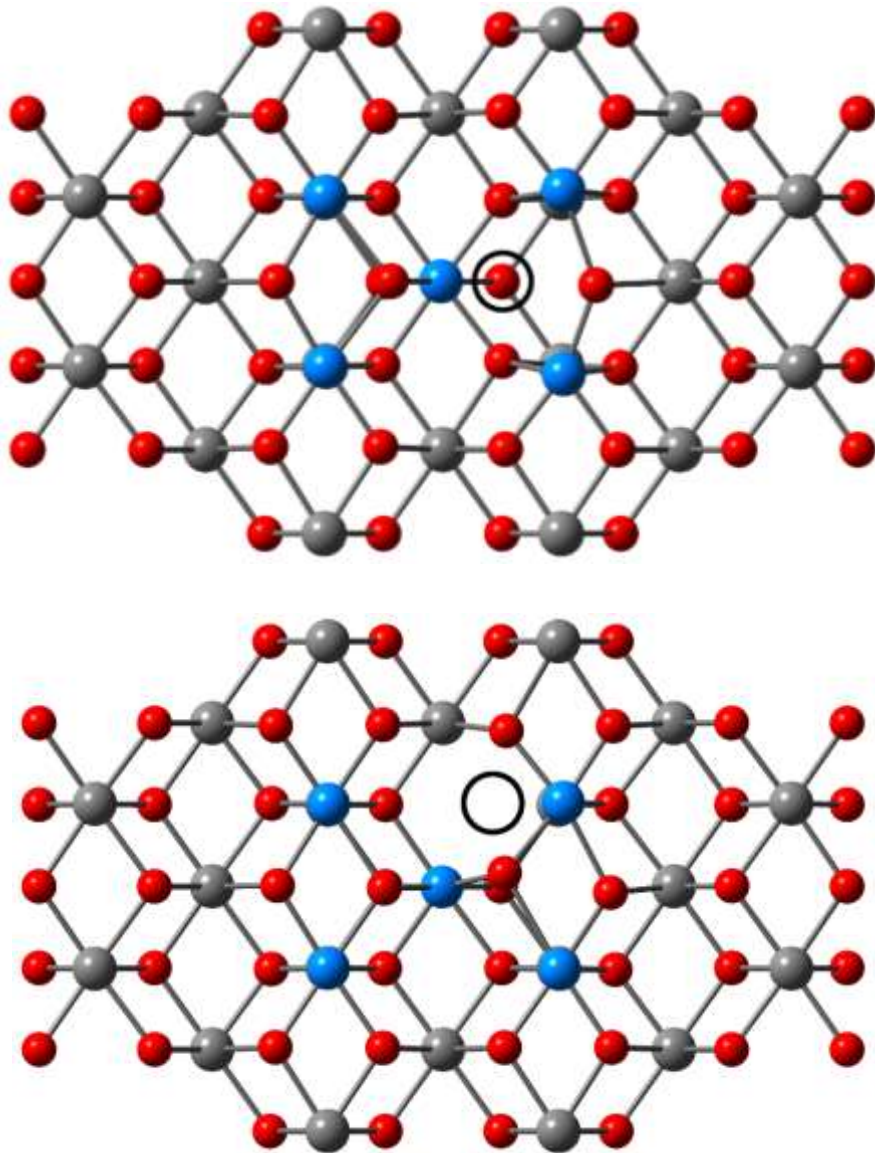


Figure 2 $U_5U_{20}O_{49}$ cluster containing an oxygen vacancy in the 1st oxygen layer (top) and 2nd layer (bottom). The cluster is viewed perpendicular to the {110} surface. Oxygen atoms are shown in red and actinide atoms in blue and grey. Grey spheres represent actinide atoms treated with 5f-in-core PPs. The position of the oxygen vacancy is indicated with a black circle. Embedding ions not shown.

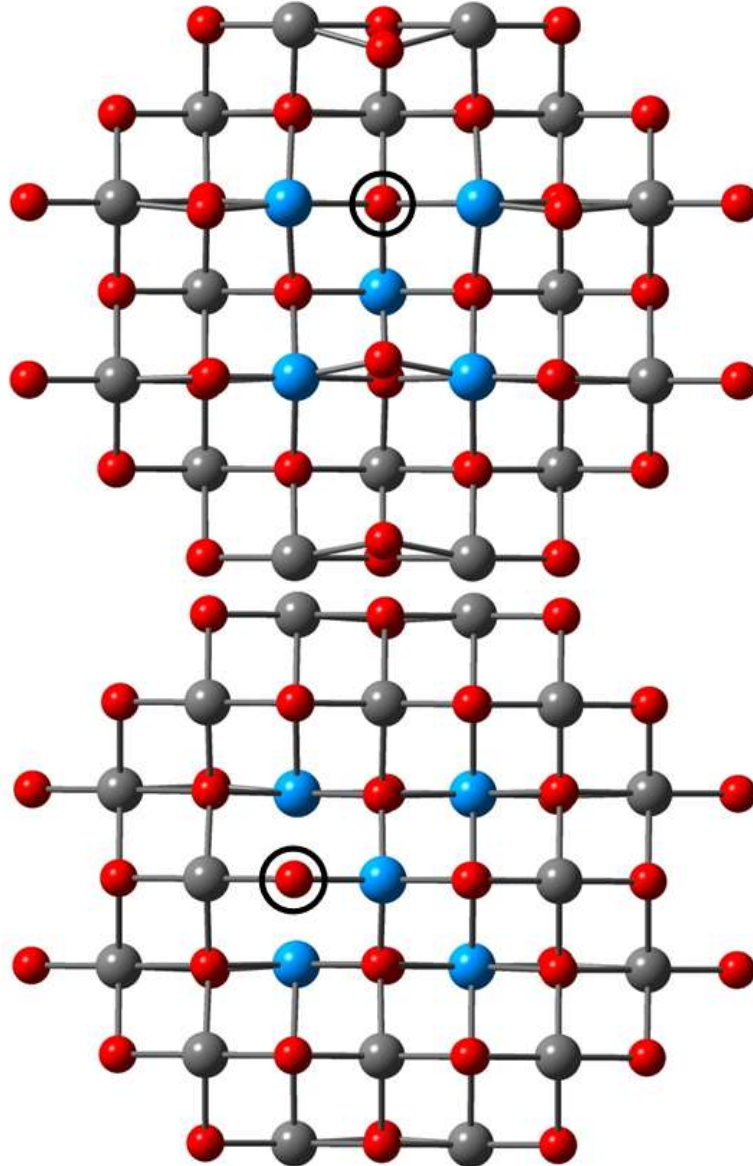


Figure 3 $U_5U_{16}O_{41}$ cluster containing an oxygen vacancy in the 1st oxygen layer (top) and 2nd layer (bottom). The cluster is viewed perpendicular to the $\{100\}$ surface. Oxygen atoms are shown in red and actinide atoms in blue and grey. Grey spheres represent actinide atoms treated with 5f-in-core PPs. The position of the oxygen vacancy is indicated with a black circle. Embedding ions not shown.

The introduction of an oxygen vacancy was found to cause some significant movement of nearby atoms. The average displacements of the nearest neighbour atoms from the oxygen vacancy are shown in the upper part of Figure 4, negative values indicate movement of the atoms away from the oxygen vacancy, while positive values indicate movement towards the vacancy.

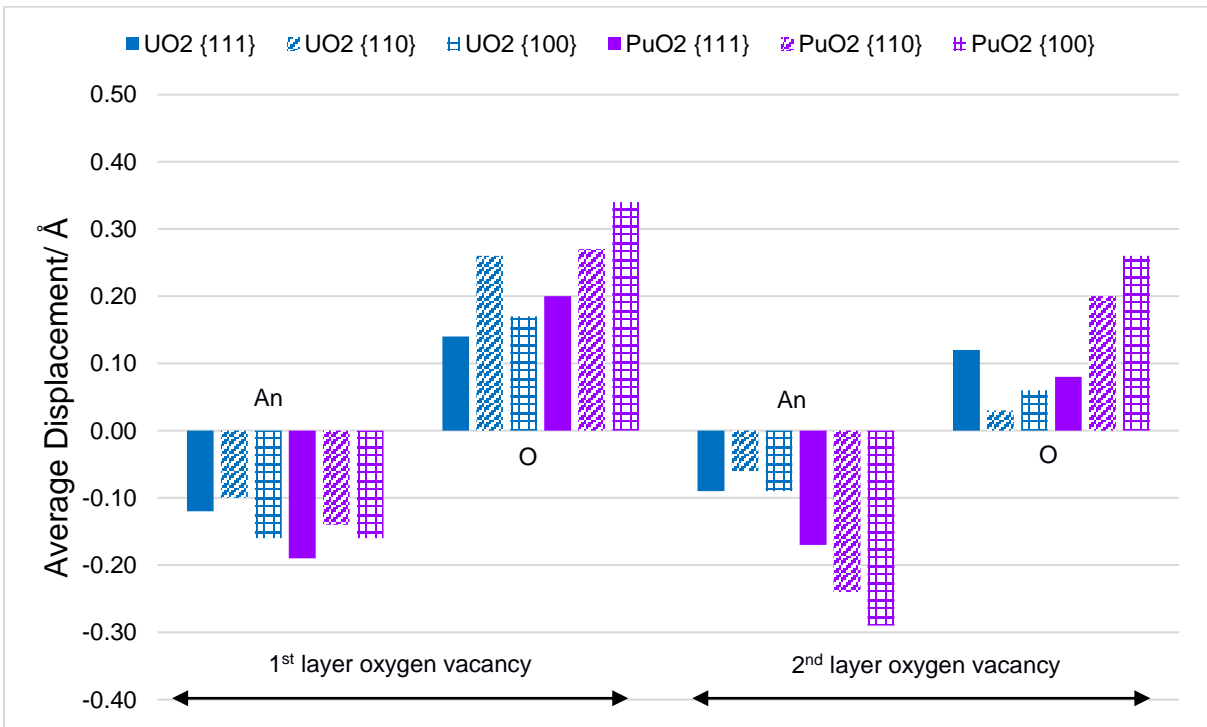
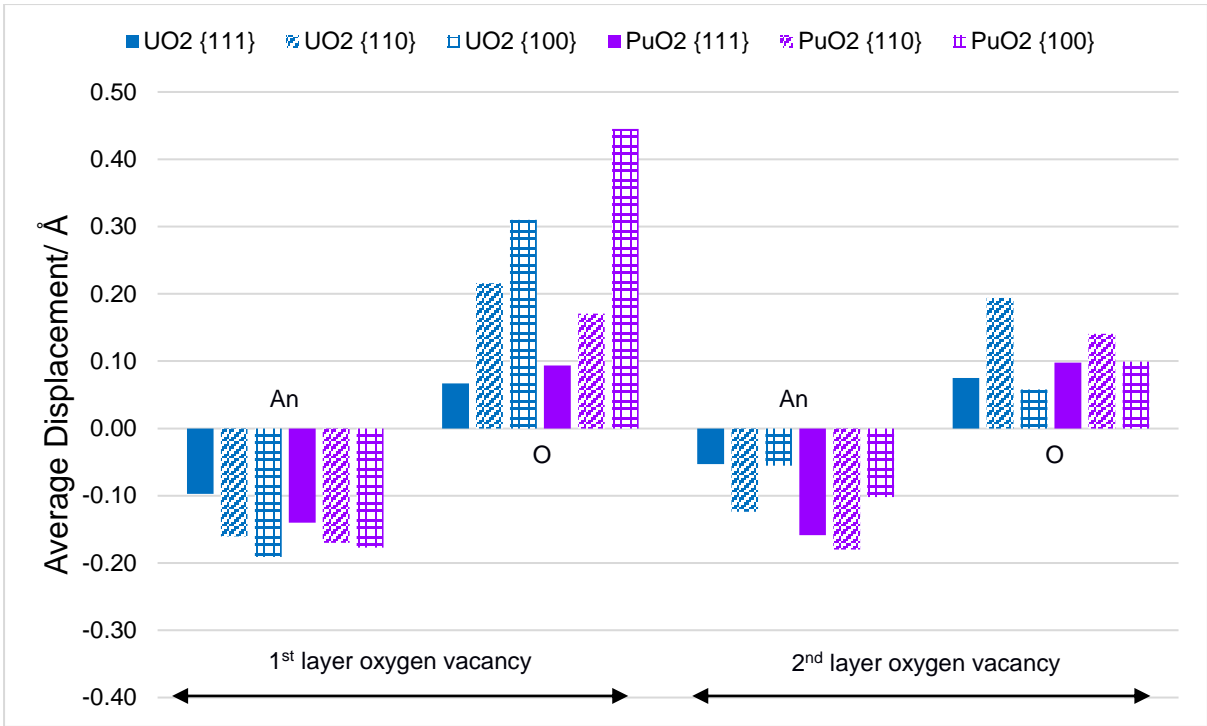


Figure 4 Average displacement of nearest neighbour atoms (either An or O) from the oxygen vacancy compared to the stoichiometric cluster. Positive displacements indicate movement towards the vacancy site, while negative displacements indicate movement away. Top graph shows results obtained using the PEECM, whereas the bottom graph shows those calculated from the periodic boundary condition calculations.

The nearest neighbour actinide atoms move away from the oxygen vacancy site; with the removal of an oxygen atom, the surrounding actinide ions are no longer shielded from each other, and hence repel each other. The nearest neighbour oxygen atoms, meanwhile, move towards the oxygen vacancy. Previous studies of oxygen vacancies in UO_2 ³⁶ and CeO_2 ²⁶ have found similar types of displacement of the nearest neighbour ions.

Larger oxygen atom displacements are seen on the 1st layer of the {110} surface than the {111}. On the {110}, an oxygen vacancy in the 1st layer (top Figure 2), causes the adjacent oxygen atom (to the right of said vacancy) to move significantly (0.30–0.40 Å) towards the vacancy, causing the large displacements seen in Figure 4 compared to the {111} surfaces. Some of the largest atomic displacements observed are those of the oxygen atoms in the 1st layer of the {100} surface. This is likely inherent to the way in which the {100} cluster is constructed, as the surface oxygen atoms here are only two-coordinate and as such are more easily distorted by the attractive pull of a vacancy. This is demonstrated in the top image of Figure 3, where the nearby oxygen atoms move significantly (approx. 0.3 Å) towards the defect site.

Actinide displacements are generally larger on the PuO_2 than the UO_2 surfaces. This is also true for the oxygen displacements on the {111} and {100} surfaces.

(ii) **Periodic calculations**

For the periodic calculations an oxygen vacancy in either the outermost or second outermost layer was created on equivalent sites on each side of the slab and the whole system was allowed to relax. The resulting geometries for the outermost case, viewed from above, can be seen in Figure 5, 6 and 7. As with the embedded cluster calculations, the neighbouring actinide ions relax away from the oxygen vacancy for both the first and second layer vacancies (Figure 4), and the surrounding oxygen sub-lattice also behaves the same in both periodic and embedded cluster approaches, relaxing towards the vacancy.

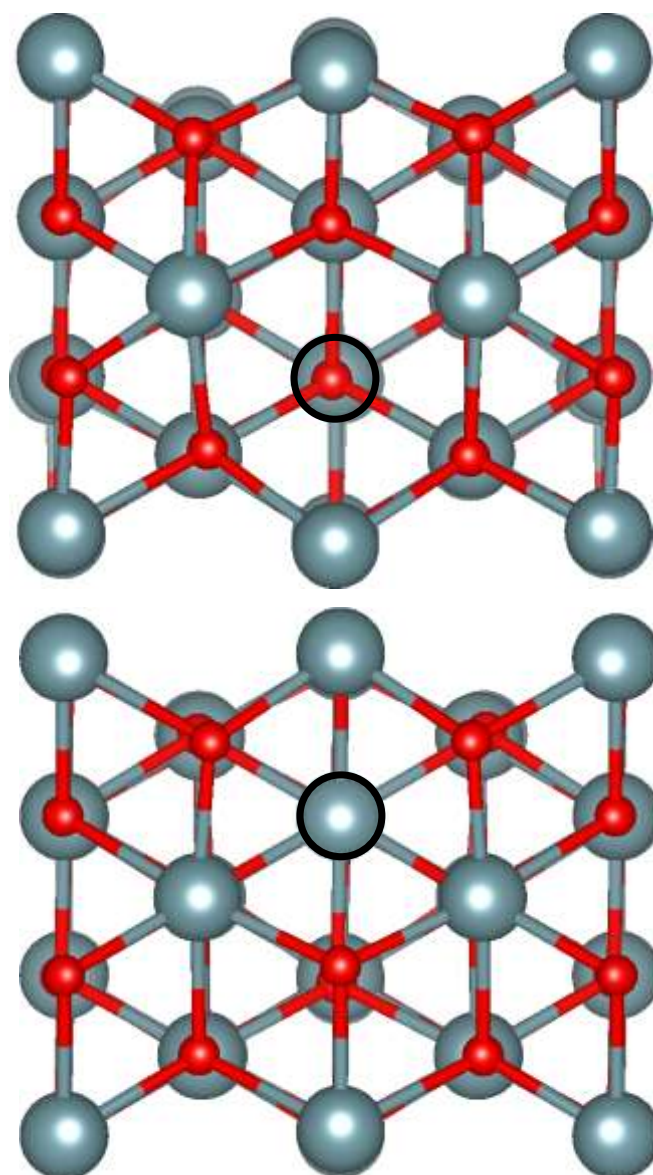


Figure 5 Oxygen vacancy geometries for the AnO₂ {111} surface, seen from above. Actinide atoms are light grey, and oxygen atoms are red. The oxygen vacancy is indicated by the black circle. The top image shows the first layer vacancy, and the bottom image shows the second layer vacancy.

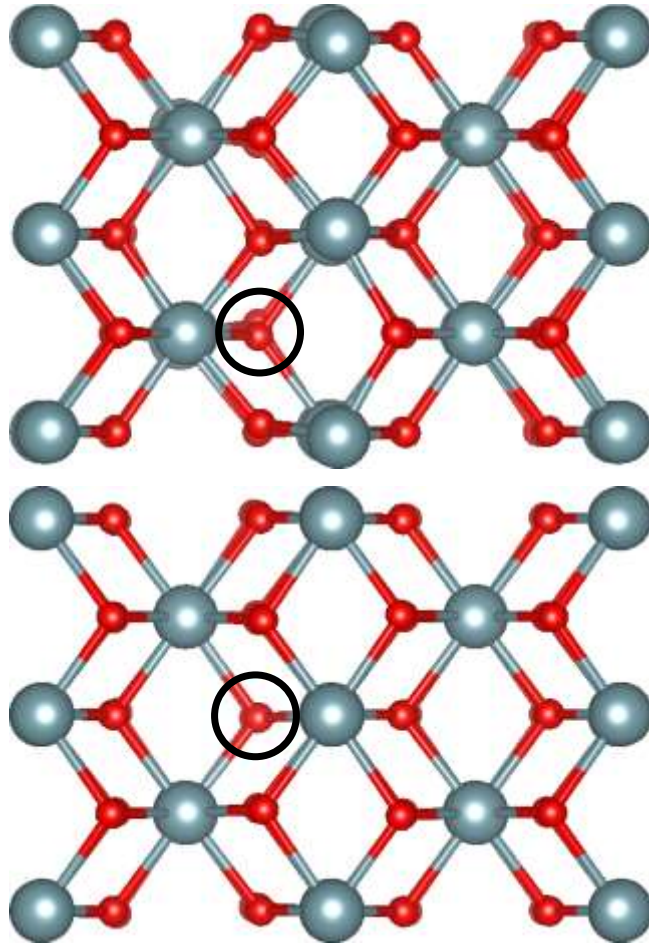


Figure 6: Oxygen vacancy geometries for the AnO₂ {110} surface, seen from above. Actinide atoms are light grey, and oxygen atoms are red. The oxygen vacancy is indicated by the black circle. The top image shows the first layer vacancy and the bottom image shows the second layer vacancy

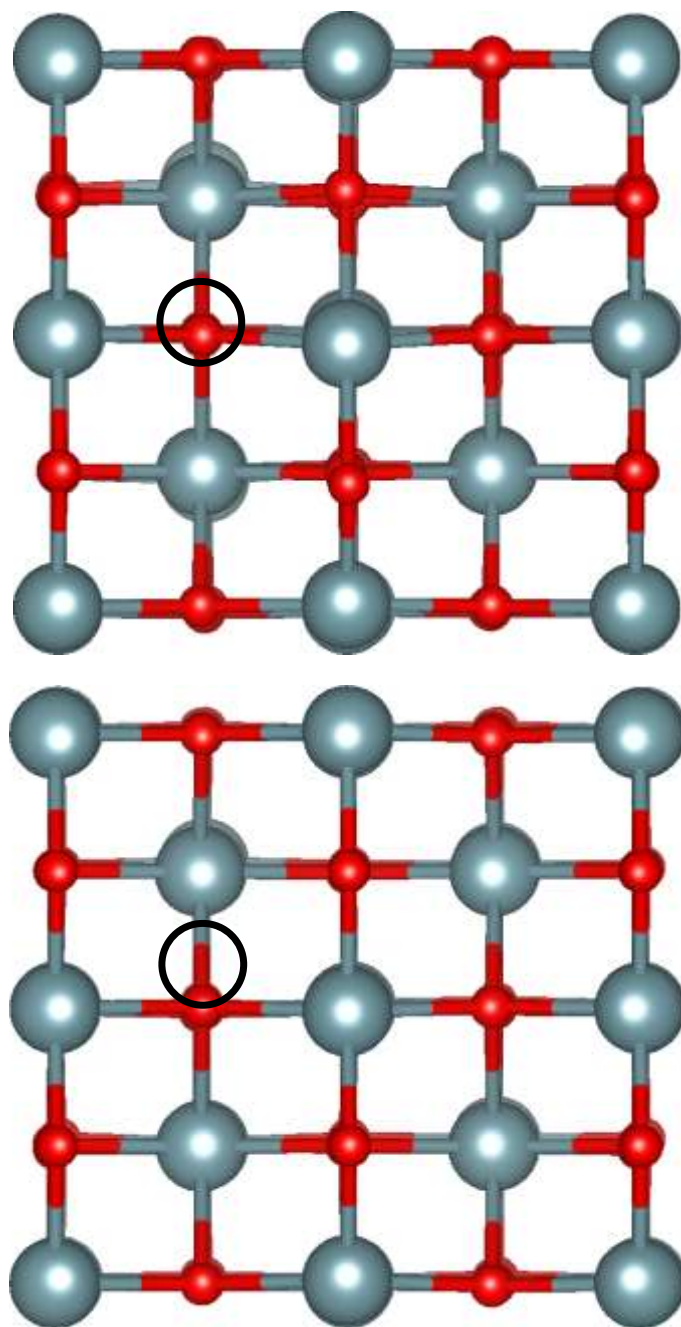


Figure 7: Oxygen vacancy geometries for the AnO₂ {100} surfaces, seen from above. Actinide atoms are light grey, and oxygen atoms are red. The oxygen vacancy is indicated by the black circle. The top image shows the first layer vacancy and the bottom image shows the second layer vacancy.

B Oxygen vacancy formation energies

Oxygen vacancy formation energies were calculated for our three target surfaces, using both embedded cluster and periodic DFT. These results are collected in Table 2 for both AnO₂ species. The embedded cluster energies at the UO₂ {111} surface are in good agreement with the periodic DFT data of Bo *et al.* who, as noted earlier,

calculated energies of 5.95 eV in the first layer and 6.08 eV in the second layer.³² Our periodic DFT gives slightly higher 1st layer vacancy formation energies. For the UO₂ {110} surface we again see that our periodic DFT gives a larger value than the embedded cluster approach. Our data bracket those of Bo *et al.*, who find 5.38 eV for the UO₂ {110} 1st layer. The embedded cluster calculations reveal a much greater difference in the formation energies between the {110} 1st and 2nd layers than for {111}, with a vacancy being 1.28 eV more stable in the 1st layer. Note that Bo *et al.* find 5.59 eV for the second {110} layer.³²

Surface	Layer	PEECM		PBE+ <i>U</i>	
		UO ₂	PuO ₂	UO ₂	PuO ₂
{111}	1 st	5.92	3.63	6.45	3.35
	2 nd	5.93	3.93	6.14	3.40
{110}	1 st	5.15	2.38	5.69	2.49
	2 nd	6.43	4.27	6.25	2.75
{100}	1 st	4.96	1.96	5.93	2.50
	2 nd	6.85	5.48	6.22	3.27

Table 2 Oxygen vacancy formation energies (eV) of the {111}, {110} and {100} surfaces of UO₂ and PuO₂ from embedded cluster (PEECM) and periodic DFT (DFT+*U*).

For both embedded cluster and PBE+*U*, oxygen vacancies on PuO₂ surfaces are in all cases calculated to be easier to form than on UO₂ surfaces, which agrees with previous theoretical calculations on bulk AnO₂ systems (see

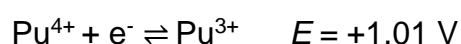
Table 1). The values calculated here for the oxygen vacancy formation energy on PuO₂ surfaces are larger than those calculated by Sun *et al.*, although they also found a much lower formation energy on the {110} than the {111} surface.⁴⁶

On CeO₂ surfaces small differences (0.01–0.18 eV) have been calculated between 1st and 2nd layer oxygen vacancy formation energies on the {111} surface,^{40,61,62} in agreement with the results here (some studies even calculate the 2nd layer vacancy to be more stable).^{40,42} In addition, scanning tunnelling microscopy studies of the CeO₂ {111} surface have found almost equal concentrations of surface and subsurface oxygen vacancies on slightly reduced surfaces, indicating a similar formation energy for both.⁶² On the {110} surface, however, larger differences have

been noted between 1st and 2nd layer oxygen vacancies formation energies, with energies differing by 0.91–1.44 eV,^{40,63} again this agrees with the results calculated here for both UO₂ and PuO₂.

In both the embedded cluster and the DFT+*U* study it is much easier to produce an oxygen vacancy in the first layer of the {110} surface than the {111}; this is likely due to the lower coordination number (CN) of the 1st layer actinide on the {110} surface (6) vs the {111} (7). This has also been noted on CeO₂ surfaces, where the coordination numbers at the surfaces are the same as in AnO₂.^{42,43,47} By contrast it is generally easier to produce an oxygen vacancy in the 2nd layer on the {111} surface than the {110} – in the second layer the oxygen atoms are fully coordinated on both surfaces. Using the embedded cluster approach, this trend follows through to the {100} surfaces: with oxygen vacancies even easier to produce in the 1st layer when compared with the {110} surface, and conversely harder to produce in the 2nd layer.

The difference in oxygen vacancy formation energies between UO₂ and PuO₂ is most likely due to the different redox properties of the two actinides. As mentioned previously, two electrons are left behind when an oxygen vacancy is formed, and these electrons reduce the nearby metal ions. The reduction potential of Pu⁴⁺ is very different from that of U⁴⁺.⁶⁴



i.e. Pu⁴⁺ is much more readily reduced than U⁴⁺, leading to lower oxygen vacancy formation energies. Note that the reduction potential for Ce⁴⁺ ($E = +1.72 \text{ V}$)⁶⁴ is even higher than that for Pu⁴⁺, and cerium dioxide has an even lower oxygen vacancy formation energy than PuO₂.

Natural population analysis was performed on the embedded cluster oxygen vacancies. For those formed in the 1st layer of the PuO₂ {111}, {110} and {100} surfaces, as well as in the 2nd layer on the {111} and {100} surfaces, there is an increase in spin density of 0.83–0.94 a.u. on two plutonium atoms neighbouring the oxygen vacancy site, indicating that the two electrons left behind from the oxygen vacancy localize on these Pu atoms, reducing them from Pu⁴⁺ to Pu³⁺. For vacancies

formed in the 2nd layer of the {110} surface however, one of the electrons is localised on one Pu atom, with an increase in spin density of 0.94 a.u., while the other electron is spread across 3 Pu atoms, with increases in spin density of 0.15, 0.25, and 0.61 a.u.

On the UO₂ surfaces it is more complicated, as might be expected for the harder-to-reduce systems. For the 1st layer vacancy on the {111} surface the two electrons are spread across three uranium atoms, with increases in spin density of 0.31, 0.55, and 1.04 a.u. This is similar to results from Bo *et al.* who found that the two electrons localize on three uranium atoms near the vacancy, resulting in one U³⁺ ion and two U^{(3+ δ)+} ions.³² For the 1st layer vacancy on the {110} surface the two electrons again spread across three uranium atoms, this time with increases in spin density of 0.38, 0.52 and 0.83 a.u. However, Bo *et al.* calculated the two electrons to localize on just two neighbouring U atoms, resulting in two U³⁺ ions.³² Finally, for the 1st layer vacancy on the {100} surface there is a Pu-like increase in spin density of 0.87-0.88 a.u. on the two uranium atoms directly neighbouring the vacancy. For the second layer vacancies the electrons are spread across four uranium atoms, with increases in spin density of 0.24, 0.32, 0.33, and 1.05 a.u. on the {111} surface, 0.23, 0.41, 0.51 and 1.14 a.u. on the {110} surface and 0.24, 0.28, 0.67 and 0.73 a.u. on the {100} surface. More specifically, these data suggest that for the UO₂ second layer vacancies, one electron localises on one uranium, with the remaining electron being spread over three metal sites.

Finally, for the embedded cluster calculations, we explored whether increasing the proportion of Hartree-Fock exchange in the functional employed would have an effect on the electron localisation around an oxygen vacancy. Taking the 1st layer vacancy on the UO₂ {111} surface as a test case, we performed a single point energy calculation with the BLYP functional (50% Hartree-Fock exchange vs 25% for PBE0), at the geometry optimised with the PBE0 functional. There was little effect on the electron localisation, with increases in spin density of 0.36, 0.48 and 1.12 a.u. on the uranium ions surrounding the vacancy, similar to the increases seen with PBE0.

C Water adsorption on the substoichiometric {111} surface

(i) Geometries - embedded cluster calculations

To investigate how oxygen vacancies impact water adsorption on the {111} surface we took the substoichiometric cluster $U_{19}O_{37}$, where the oxygen vacancy is in the 1st layer (Figure 1, left), and adsorbed water either molecularly (in 2 different ways, as discussed below) or dissociatively.

For the first molecular adsorption, a water molecule was placed in the same geometry as that optimized on the stoichiometric surface, but with one of the closest surface oxygen sites now being vacant (Figure 8). After geometry optimization, the $U-O_w$ bond length is 2.61 Å (O_w indicates an oxygen from a water molecule), slightly longer than for adsorption on the stoichiometric surface (2.57 Å).¹ This is 0.05 Å shorter than that calculated by Bo *et al.* with periodic DFT+ U , who also found a shortening of the $U-O_w$ bond length going from the stoichiometric to substoichiometric surfaces (by 0.05 Å).³² The $H-O_s$ distance is 1.60 Å, significantly shorter than that found on the stoichiometric surface (1.76 Å, O_s indicating a surface oxygen species). This is also significantly shorter than the 1.71 Å calculated by Bo *et al.*, who actually found the $H-O_s$ distance to lengthen by 0.10 Å on going from the stoichiometric to substoichiometric surface.

For the second type of molecular adsorption on the {111} cluster the water molecule was placed above the oxygen vacancy, with the hydrogen atoms pointing away from the surface. This geometry had also been found in the periodic DFT study of Bo *et al.*³² Upon geometry optimization the water molecule moves slightly off the centre of the oxygen vacancy site and optimizes to a position between two uranium atoms adjacent to the oxygen vacancy site (Figure 9). The two $U-O_w$ distances are 2.65 Å and 2.86 Å, the shorter being similar to the $U-O_w$ distance for the first type of molecular adsorption. As the hydrogen atoms are pointing away from the surface there is no hydrogen bonding between the water molecule and the surface, unlike for water adsorbing above a uranium atom. The oxygen atom of the water molecule sits 1.07 Å above the oxygen vacancy, close to the 1.13 Å calculated by Bo *et al.*³²

For dissociative adsorption we initially placed an OH group above the oxygen vacancy, with a hydrogen atom above an adjacent oxygen site (Figure 10). After

optimisation, the two OH groups both have O-H bond lengths of 0.97 Å, slightly different from our previous results on the stoichiometric surface, where one OH group has a bond length of 0.96 Å and the other is slightly longer at 1.01 Å.¹ The two groups lie slightly above the plane of the surface, with U-OH lengths ranging from 2.50–2.73 Å compared with 2.30–2.50 Å on the stoichiometric cluster, and the oxygen atoms in the OH groups moving by 0.46 Å in the z direction (the z direction defined as the normal to the surface), compared with their positions in the stoichiometric cluster.

The two types of molecular adsorption were also investigated on the PuO₂ {111} vacancy surface. As described for UO₂ above, the geometry of the water molecule on the stoichiometric surface was initially taken, and then optimized on the substoichiometric cluster at a surface oxygen site adjacent to the vacancy. However, on the PuO₂ surface this water molecule optimized to the dissociative configuration.

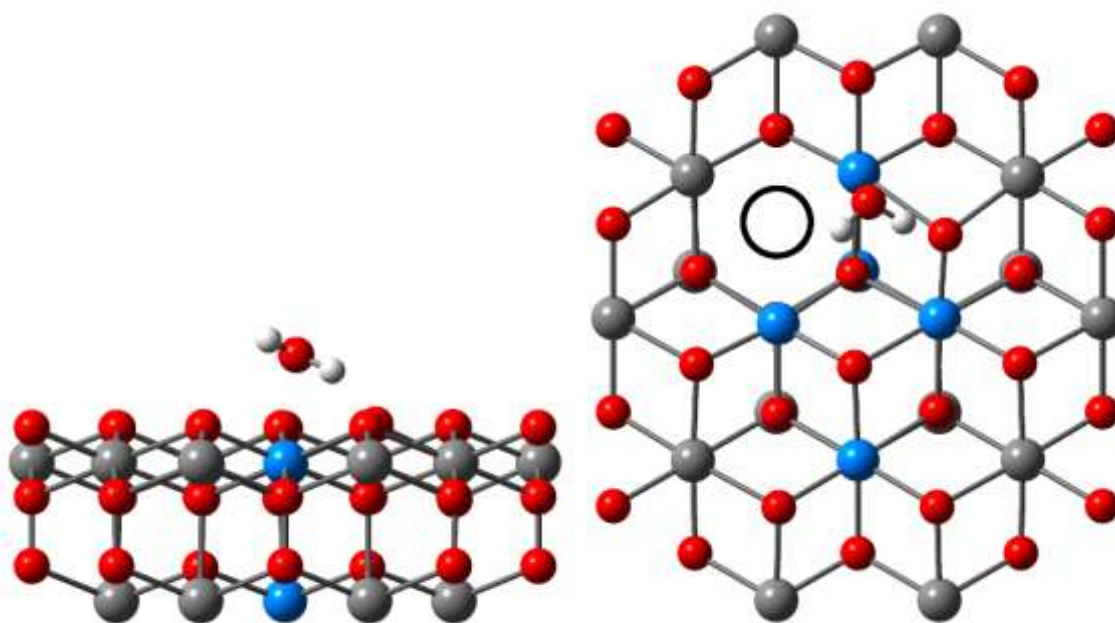


Figure 8 Molecular adsorption of a single water molecule on the {111} surface of a U₅U₁₄O₃₇ cluster. Top view shows the cluster in the plane of the surface, while the bottom view is perpendicular to the surface. Hydrogen atoms are shown in white, oxygen atoms in red and actinide atoms in blue and grey. Grey spheres represent actinide ions treated with 5f-in-core PPs. The position of the oxygen vacancy is indicated with a black circle. Embedding ions not shown.

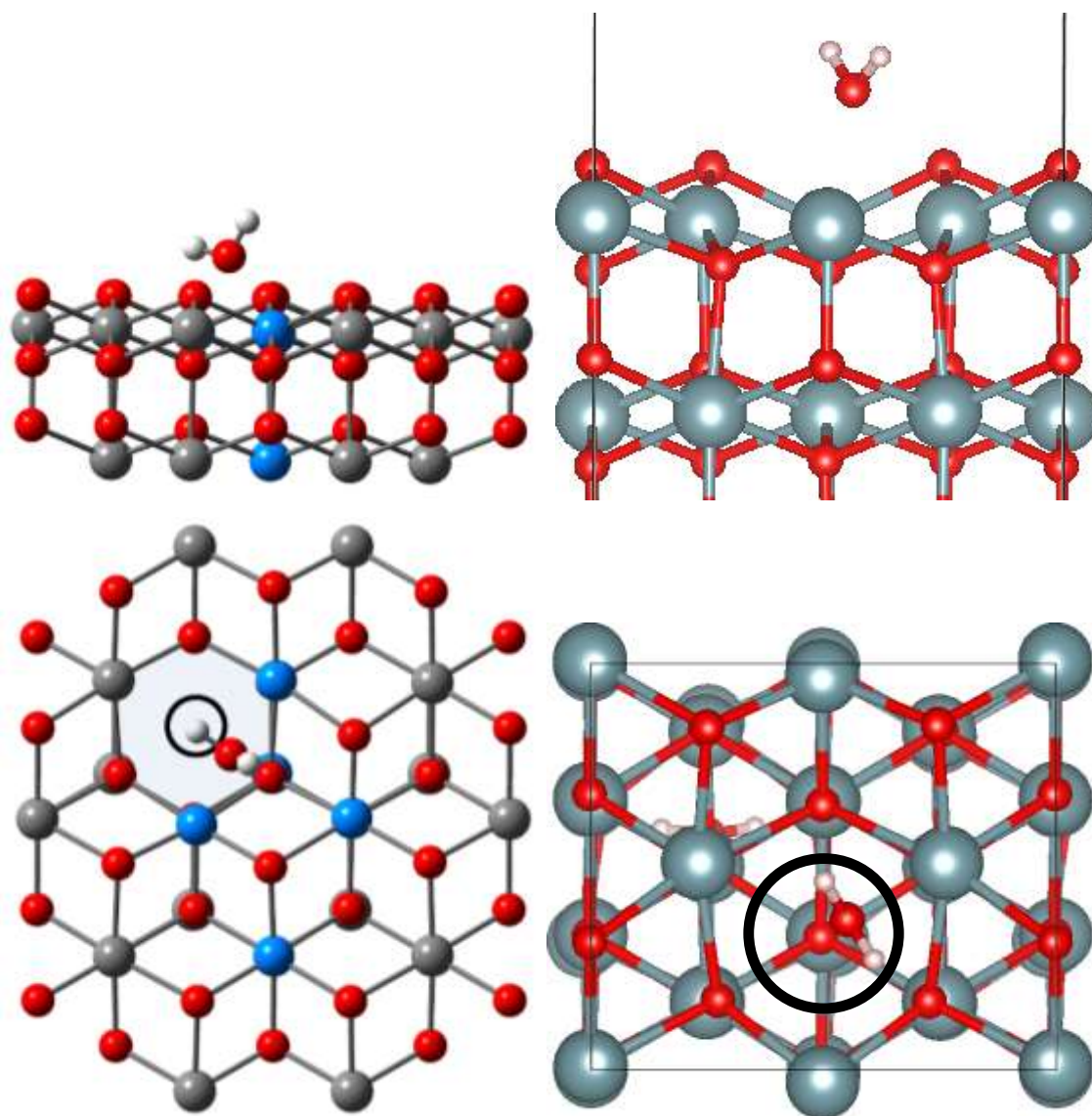


Figure 9 (left) Molecular adsorption of a single water molecule on the {111} surface of a U₅U₁₄O₃₇ embedded cluster above the oxygen vacancy. Top panel shows the cluster in the plane of the surface, while the bottom panel is perpendicular to the surface. Hydrogen atoms are shown in white, oxygen atoms in red and actinide atoms in blue and grey. **(right)** Molecular adsorption of a single water molecule on the UO₂ {111} slab, above the oxygen vacancy. The top panel shows the side-on view of half the slab and the bottom panel shows the view from above. Hydrogen atoms are shown in white, oxygen atoms in red and uranium atoms in grey. The position of the oxygen vacancy is indicated with a black circle.

For the second type of molecular adsorption, a water molecule was placed above the oxygen vacancy on the PuO₂ {111} cluster; upon geometry optimization the water molecule moved to lie between two surface actinide ions towards the edge of the cluster (Figure 11). The adsorption geometry is similar to that on the UO₂ {111} surface; on the PuO₂ surface the Pu-O_w distances are 2.65 Å and 2.97 Å, compared with 2.65 Å and 2.86 Å on UO₂.

Dissociative adsorption occurs in a similar way on the PuO₂ surface as for the UO₂, again the two OH groups have O-H lengths of 0.97 Å. Also as on UO₂ the OH groups lie above the plane of the surface, with Pu-O distances lengthening from 2.27–2.45 Å on the stoichiometric surface to 2.48–2.65 Å on the substoichiometric surface. The lengthening is due in part to the movement of the OH groups above the surface, with the oxygen atoms lying 0.44–0.46 Å higher in the z direction than on the stoichiometric surface.

(ii) Geometries – periodic calculations

A substoichiometric slab where the oxygen vacancy is in the outermost layer was used to investigate water adsorption on the {111} surface of both UO₂ and PuO₂. Molecular and dissociative adsorption on or near an oxygen vacancy were both investigated. For molecular adsorption a water molecule was placed near the vacancy before a geometry optimisation was performed, on both UO₂ (Figure 9) and PuO₂ (Figure 11). Only the type of molecular adsorption shown was found to be stable in this case. For dissociative adsorption the OH-group was placed at the vacancy and the remaining hydrogen adsorbed on a neighbouring oxygen atom (Figure 10, for a UO₂ example). PuO₂. Vacancies and adsorbates were introduced on both sides, hence the extra water molecules can be seen on in the bottom right panels of Figure 9 and Figure 11.

As for the embedded cluster case, for molecular adsorption we find that the An-O_w distances increase during relaxation compared to the stoichiometric case, with the U-O_w distance increasing from 2.62 to 2.90 Å and the Pu-O_w distance increasing from 2.58 to 2.92 Å. For dissociative adsorption, the An-O_sH distances also increase compared to the stoichiometric case, with the U-O_sH distance increasing from 2.41 to 2.65 Å and the Pu-O_w distance increasing from 2.36 to 2.57 Å.

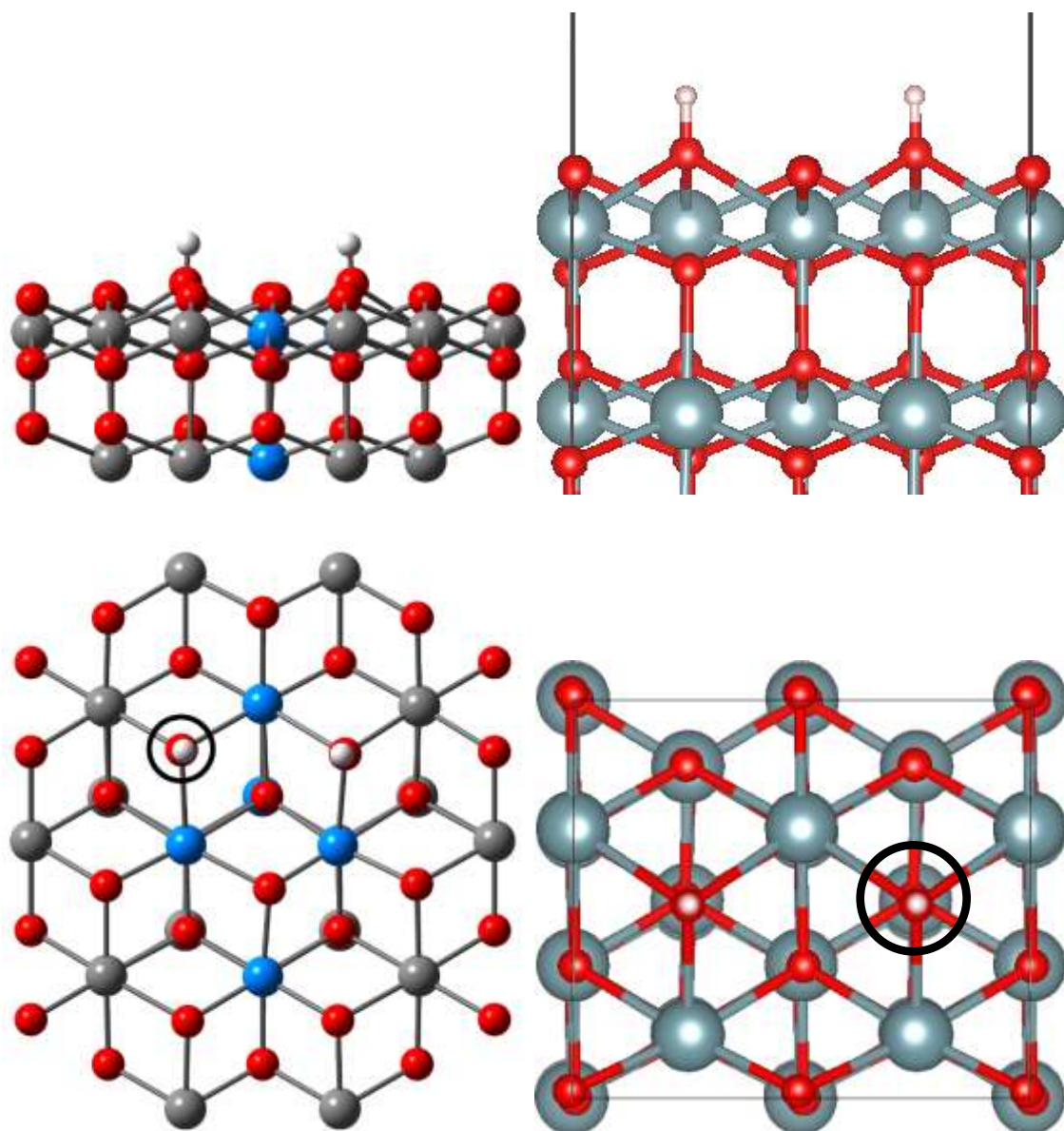


Figure 10 (left) Dissociative adsorption of a single water molecule on the {111} surface of a $U_5U_{14}O_{37}$ embedded cluster. Top view shows the cluster in the plane of the surface, while the bottom view is perpendicular to the surface. Hydrogen atoms are shown in white, oxygen atoms in red and actinide atoms in blue and grey. **(right)** Dissociative adsorption of a single water molecule on the UO_2 {111} slab, at the oxygen vacancy. The top panel shows the side-on view of half the slab and the bottom panel shows the view from above. Hydrogen atoms are shown in white, oxygen atoms in red and uranium atoms in grey. The position of the oxygen vacancy is indicated with a black circle.

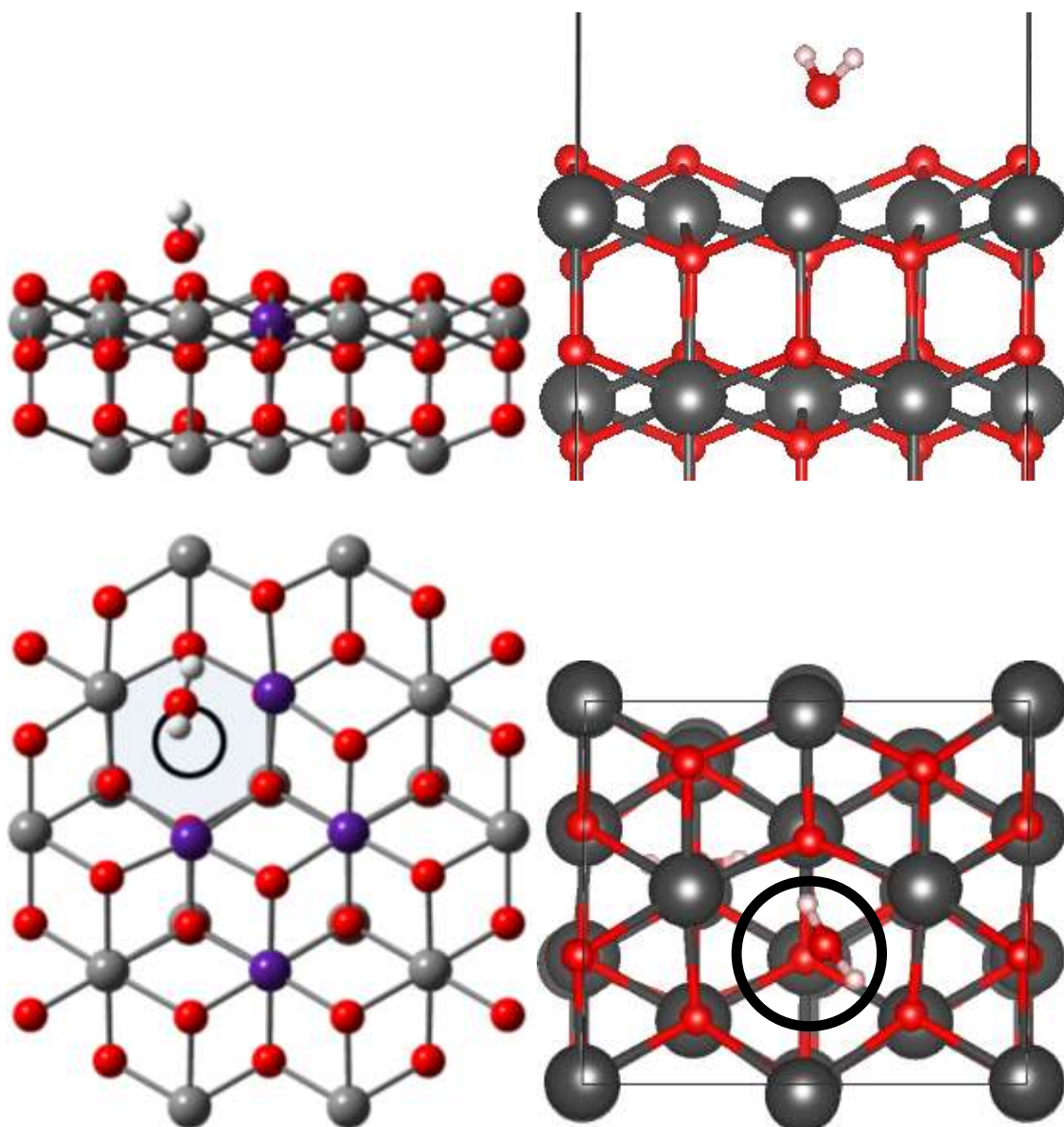


Figure 11 (left) Molecular adsorption of a single water molecule on the {111} surface of a $\text{Pu}_5\text{Pu}_{14}\text{O}_{37}$ cluster above the oxygen vacancy. Top view shows the cluster in the plane of the surface, while the bottom view is perpendicular to the surface. Hydrogen atoms are shown in white, oxygen atoms in red and plutonium atoms in purple and grey. **(right)** Molecular adsorption of a single water molecule on the PuO_2 {111} slab, above the oxygen vacancy. The top panel shows the side-on view of half the slab and the bottom panel shows the view from above. Hydrogen atoms are shown in white, oxygen atoms in red and plutonium atoms in dark grey. The position of the oxygen vacancy is indicated with a black circle.

(iii) Energies

Adsorption energies for the two types of molecular adsorption, and dissociative adsorption, on the UO_2 and PuO_2 {111} surfaces containing an oxygen vacancy are shown in Table 3.

Adsorption Type	Embedded cluster		Periodic	
	UO ₂	PuO ₂	UO ₂	PuO ₂
Molecular1 ^a	-0.58	–	–	–
Molecular2 ^b	-0.61	-0.81	-0.90	-0.60
Dissociative	-1.93	-2.51	-2.23	-2.10

Table 3 Water adsorption energies (eV) on the reduced UO₂ and PuO₂ {111} surfaces from both embedded cluster and periodic DFT. ^a Molecular1 adsorption occurs with the water molecule adsorbing above the actinide ion, as shown in Figure 8. ^b Molecular2 adsorption occurs with the water molecule adsorbing above the vacancy, as shown in Figure 9 and Figure 11.

For the embedded cluster calculations, the energy of molecular adsorption on the UO₂ {111} surface increases slightly from the stoichiometric surface;¹ 0.06 eV or 0.09 eV for the two types of molecular adsorption. At the periodic DFT level, a more significant, but still fairly modest, increase vs the stoichiometric surface² is predicted, 0.37 eV, for adsorption above the vacancy. This is similar to the work of Bo *et al.*, who predict 0.27 eV and 0.33 eV increases vs the stoichiometric UO₂ {111} surface for the two types of molecular adsorption.³² There is a more significant increase for molecular adsorption on the PuO₂ surface at the embedded cluster level, 0.28 eV, slightly larger than the 0.15 eV increase predicted by our periodic DFT.

Hence all approaches predict a modest increase in molecular adsorption energy on the vacancy {111} surfaces. Similar agreement is seen for dissociative adsorption, but here the magnitude is substantially larger. At the embedded cluster level we find increases of 1.30 eV and 2.06 eV respectively vs the stoichiometric UO₂ and PuO₂ {111} surfaces. PBE+*U* predicts increases of 1.73 eV for UO₂ and 1.78 eV for PuO₂, the former being similar to that found by Bo *et al.* (1.52 eV). The much larger increases seen for the dissociative case arise because the hydroxyl formed from the dissociation of the water molecule sits in the oxygen vacancy site, hence increasing the coordination numbers of the nearby actinide ions.

For the embedded cluster calculations, we note that, as for the stoichiometric surface,¹ the inclusion of dispersion with the D3 parameters (data not shown) does not change the ordering of energies on the substoichiometric surface. There is a greater increase in adsorption energies on the PuO₂ than UO₂ cluster; the energies

are increased by 0.16–0.20 eV on the UO_2 cluster, and by 0.25–0.26 eV on the PuO_2 cluster, vs the data presented in Table 3.

D Water adsorption on the substoichiometric {110} surface

(i) Geometries - embedded cluster calculations

The substoichiometric cluster $\text{U}_{25}\text{O}_{49}$, where the oxygen vacancy is in the 1st layer, was used to investigate both molecular and dissociative water adsorption on the {110} surface. For molecular adsorption, a water molecule was initially placed in the same position as in the stoichiometric cluster. After geometry optimisation, the water molecule lies adjacent to the oxygen vacancy; the optimized structure is shown in Figure 12. The $\text{U}-\text{O}_w$ bond length is 2.65 Å, the same length as on the stoichiometric surface, and very close to that found by Bo *et al.*'s periodic DFT, 2.64 Å.³² The O_s-H bond lengths are 1.80 Å and 1.94 Å, compared to 1.78 Å and 2.13 Å on the stoichiometric surface; the Bo *et al.* study found the shorter O-H bond length to be 1.74 Å.³² Molecular adsorption occurs in a similar way on the substoichiometric PuO_2 {110} surface, with a $\text{Pu}-\text{O}_w$ distance of 2.65 Å and O_s-H distances of 1.80 Å and 1.84 Å; all of these distances are slightly longer than on the stoichiometric surface, by 0.11 Å, 0.07 Å, and 0.16 Å respectively.

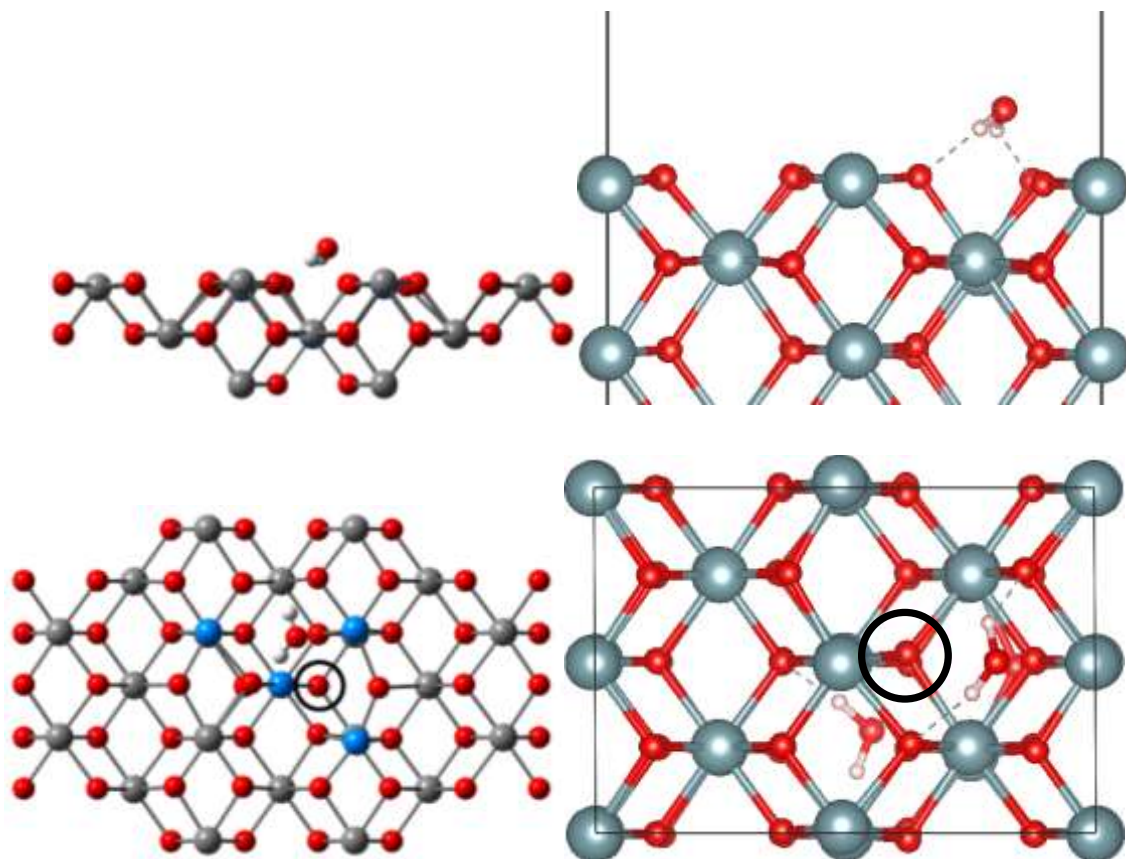


Figure 12 (left) Molecular adsorption of a single water molecule on the {110} surface of a $\text{U}_5\text{U}_{20}\text{O}_{49}$ embedded cluster. Top view shows the cluster in the plane of the surface, while the bottom view is perpendicular to the surface. Hydrogen atoms are shown in white, oxygen atoms in red and actinide atoms in blue and grey. **(right)** Molecular adsorption of a single water molecule on the UO_2 {110} slab, near the oxygen vacancy. The top panel shows the side-on view of half the slab and the bottom panel shows the view from above. Hydrogen atoms are shown in white, oxygen atoms in red and uranium atoms in light grey. Dashed lines are hydrogen bonds. The position of the oxygen vacancy is indicated with a black circle.

For dissociative adsorption two initial structures were investigated, following Bo *et al.*³² For the first, an OH group was placed at the oxygen vacancy site, while an additional hydrogen atom was placed above an adjacent surface oxygen site (Figure 13). After optimisation, the O-H bond lengths of the surface hydroxyls are 0.99 and 1.00 Å, almost unaltered vs the stoichiometric surface (0.98 Å). The oxygens of the hydroxyls lie above the surface slightly being 0.20 Å and 0.25 Å higher than an oxygen atom in the bulk terminated surface. The two hydroxyls point away from each other such that there is minimal interaction between them. A similar geometry is found on the PuO₂ {110} surface, with the oxygens of the hydroxyls lying 0.21 Å and 0.22 Å higher than an oxygen atom in the bulk terminated surface.

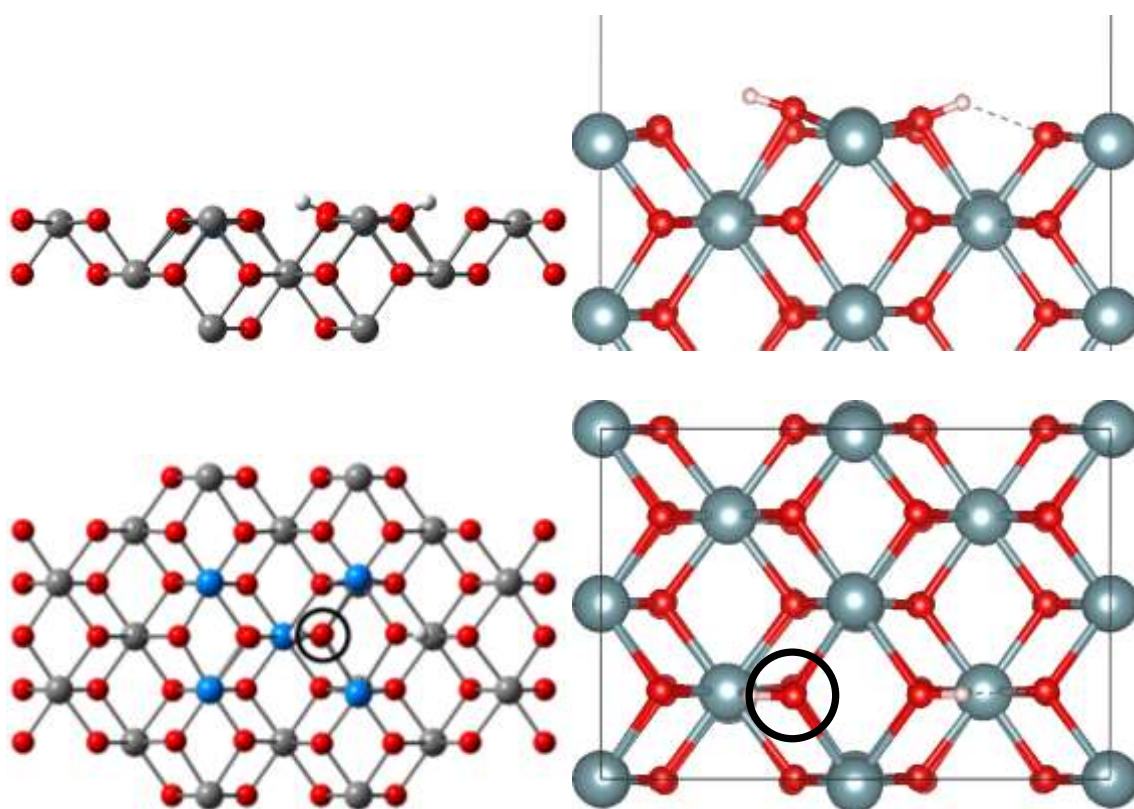


Figure 13 (left) Dissociative adsorption of a single water molecule on the {110} surface of a U₅U₂₀O₄₉ embedded cluster. Top view shows the cluster in the plane of the surface, while the bottom view is perpendicular to the surface. Hydrogen atoms are shown in white, oxygen atoms in red and uranium atoms in blue and grey. The position of the oxygen vacancy is indicated with a black circle. **(right)** Dissociative adsorption of a single water molecule on the UO₂ {110} slab, at the oxygen vacancy. The top panel shows the side-on view of half the slab and the bottom panel shows the view from above. Hydrogen atoms are shown in white, oxygen atoms in red and uranium atoms in light grey. Dashed lines are hydrogen bonds. The position of the oxygen vacancy is indicated with a black circle.

The second dissociative structure involved placing the hydroxyl group in the same position, but this time placing the additional hydrogen on the other adjacent surface

oxygen site (Figure 14). In this geometry a hydrogen bond is formed between the two hydroxyl groups, with an OH-OH distance of 1.63 Å. The oxygen atoms of these hydroxyl groups lie above the surface, being 0.36 Å and 0.67 Å higher than an oxygen atom in the bulk terminated surface. A similar geometry was also found on the Pu₅Pu₂₀O₄₉ cluster, although the OH-OH distance is shorter, at 1.55 Å. The oxygen atoms of the hydroxyl groups lie 0.17 Å and 0.73 Å higher than an oxygen atom in the bulk terminated surface.

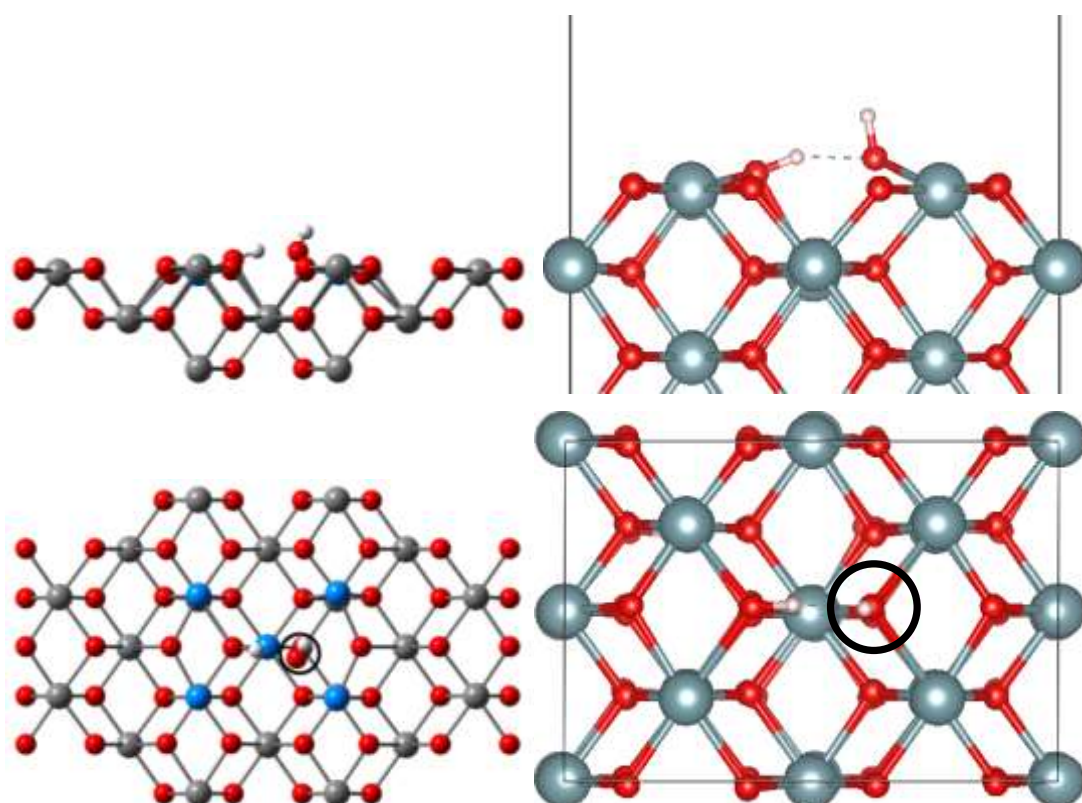


Figure 14 (left) Dissociative adsorption of a single water molecule on the {110} surface of an embedded U₅U₂₀O₄₉ cluster. Top view shows the cluster in the plane of the surface, while the bottom view is perpendicular to the surface. Hydrogen atoms are shown in white, oxygen atoms in red and actinide atoms in blue and grey. **(right)** Dissociative adsorption of a single water molecule on the UO₂ {110} slab, at the oxygen vacancy. The top panel shows the side-on view of half the slab and the bottom panel shows the view from above. Hydrogen atoms are shown in white, oxygen atoms in red and uranium atoms in light grey. Dashed lines are hydrogen bonds. The position of the oxygen vacancy is indicated with a black circle.

(ii) Geometries – periodic calculations

A substoichiometric slab where the oxygen vacancy is in the outermost layer was used to investigate water adsorption on the {110} surface. Molecular and dissociative

adsorption on or near an oxygen vacancy were both investigated. For molecular adsorption a water molecule was placed near the vacancy before a geometry optimisation was performed (Figure 12). For dissociative adsorption the OH-group was placed at the vacancy and the remaining hydrogen adsorbed on a neighbouring oxygen atom (Figures 13 and 14). Vacancies and adsorbates were again introduced on both sides, hence extra water molecules can be seen in the bottom right panel of Figure 12.

For molecular adsorption, we find that the An-O_w distances change modestly compared with the stoichiometric case, with the U-O_w distance increasing from 2.72 to 2.73 Å and the Pu-O_w distance decreasing from 2.66 to 2.60 Å. These small changes are similar to those found by the embedded cluster calculations. For dissociative adsorption, the An-O_{sH} distances also change vs the stoichiometric case; the U-O_{sH} distance increases from 2.44 to 2.62 Å whereas the Pu-O_{sH} distance decreases from 2.50 to 2.45 Å. Again, the changes are much smaller than those seen on the {111} surface.

(iii) Energies

Adsorption energies for molecular, and the two types of dissociative, adsorption on the UO₂ and PuO₂ {110} surfaces containing an oxygen vacancy are shown in

Table 4.

Adsorption Type	Embedded cluster		Periodic	
	UO ₂	PuO ₂	UO ₂	PuO ₂
Molecular	-0.81	-1.00	-0.82	-0.44
Dissociative1 ^a	-1.83	-2.29	-1.89	-1.95
Dissociative2 ^b	-1.02	-1.15	-1.50	-1.51

Table 4 Water adsorption energies (eV) on the reduced UO₂ and PuO₂ {110} surfaces from both embedded cluster and periodic DFT. ^a Dissociative1 adsorption occurs with the hydroxyl groups facing away from each other, as shown in Figure 13. ^b Dissociative2 adsorption occurs with the hydroxyl groups facing each other, as shown in Figure 14.

The adsorption energy for molecular water on the substoichiometric UO₂ {110} cluster is -0.81 eV, by contrast to -1.06 eV on the stoichiometric surface,¹ so the

adsorption energy decreases in the presence of an oxygen vacancy. This is also true from our periodic calculations, with a decrease of 0.11 eV. By contrast, Bo *et al.* find molecular adsorption to be much stronger on the substoichiometric surface, by 0.80 eV.³² However, the geometry of their molecular adsorption on the stoichiometric surface differs significantly from ours, as well as their own adsorption geometry on the substoichiometric surface: on the stoichiometric surface they find a water molecule adsorbing almost perpendicular to the surface. Their substoichiometric geometry is, however, similar to ours, and we suggest that their different (and potentially less stable) geometry on the stoichiometric surface may lead to the much greater increase in energy in the presence of a vacancy. That said, Bo *et al.*'s value of -1.42 eV is significantly larger than our value on the substoichiometric surface.

Despite all the key bond distances for molecular adsorption on the PuO_2 {110} surface increasing from the stoichiometric surface to the substoichiometric surface, there is a small increase in the adsorption energy, 0.06 eV, at the embedded cluster level. This is by contrast to our periodic DFT, which predicts a rather larger 0.44 eV increase in this adsorption on the vacancy surface.

The embedded cluster calculations indicate that the first type of dissociative adsorption on vacancy UO_2 {110}, in which the hydroxyls point away from each other, is clearly the most favoured. This leads to a modest increase of 0.23 eV compared to the stoichiometric surface. This is also true for the periodic case, leading to an increase of 0.39 eV compared to the stoichiometric slab. The second type of dissociative adsorption leads to a decrease compared with the stoichiometric surface. Although there is a hydrogen bond between the two hydroxyls, there are long U-O distances between the second hydroxyl and the actinide ions, which make this adsorption less favourable. This decrease is also found by our periodic DFT, by 0.11 eV vs the stoichiometric surface.

On substoichiometric PuO_2 {110} with the embedded cluster calculations there is a small increase in molecular adsorption energy of 0.06 eV. There is a large increase, however, in the dissociative adsorption compared to the stoichiometric surface (0.95 eV). Our periodic DFT shows an increase in dissociative adsorption energy vs the stoichiometric surface, by 0.37 eV. This is again mirrored in the periodic case, showing an increase by 0.81 eV compared to the stoichiometric slab.

Hence, as on the {111} surface, there is a large difference between the dissociative adsorption energies on UO_2 and PuO_2 , with dissociative adsorption being more favourable on the PuO_2 surface. Natural population analysis of the substoichiometric UO_2 {110} surface cluster shows that after dissociative adsorption the two electrons left behind by the oxygen vacancy are localised on two uranium atoms (with spin densities on these atoms of 2.84 and 2.97 a.u., compared to 2.04–2.27 a.u. on the remaining uranium atoms), compared to before where, as mentioned above, the electrons are spread across three atoms (with spin densities of 2.48–2.95 a.u.). There may be an energy penalty for localising the electrons in the UO_2 system when dissociative adsorption occurs (which does not happen on the PuO_2 surface, as the electrons are already localised on two Pu atoms) and so leads to the difference in adsorption energies between the UO_2 and PuO_2 surfaces. A similar effect is seen on the {111} surface, which may lead to the differences between dissociative adsorption on UO_2 and PuO_2 there too.

It is worth noting that the electron localisation does not occur with molecular adsorption on UO_2 {110}, the differences in spin density on the uranium atoms between the substoichiometric surface without water and with molecular water adsorbed are small (<0.15 a.u.) and the two electrons remain spread mainly across three uranium atoms (with spin densities on these atoms of 2.50–2.85 a.u.). There is also a much smaller difference between the adsorption energies on the UO_2 and PuO_2 surfaces.

Inclusion of dispersion corrections (data not shown) in the embedded cluster calculations increases the adsorption energies, as on the {111} surface, by 0.21–0.24 eV for UO_2 , and 0.30–0.36 eV for PuO_2 vs the data in

Table 4.

E Water adsorption on the substoichiometric {100} surface

(i) Geometries - embedded cluster calculations

For the {100} surface the substoichiometric $\text{U}_{21}\text{O}_{41}$ cluster was used, with the vacancy in the 1st layer, to investigate both molecular and dissociative adsorptions. Analogous calculations on PuO_2 {100} were attempted, but convergence difficulties were encountered and as such no data are presented here.

In the molecular case, the water molecule was initially placed near, but not directly above, the vacancy site. This was done as it maximises the amount of hydrogen bonding possible between the molecule and surface oxygen atoms. During geometry optimisation the molecule rotated as shown in Figure 15, forming a final configuration similar to that found by Bo *et al.* regarding the molecular adsorption of water onto the NpO_2 {100} surface⁵⁶. The $\text{O}_s\text{-H}$ bond length was 1.47 Å, compared to 1.45 Å in the work of Bo *et al.* whereas the $\text{O}_w\text{-H}$ bond length closest to the surface was stretched to 1.06 Å. As this is a significant extension of the $\text{O}_w\text{-H}$ bond in the direction of a surface oxygen atom, it raised the question as to whether a transition state had been located rather than a true energy minimum, and whether the adsorption configuration would be more stable if the molecule fully dissociated.

In order to investigate whether a “molecular to dissociative” configuration would be the more stable, the converged system was subjected to a second geometry optimisation with the $\text{O}_w\text{-H}$ bond extended by 0.1 Å. The result of this second optimisation is depicted in Figure 16 where, rather than returning to the original configuration, the water molecule instead fully dissociated, forming two surface hydroxyls with $\text{O}_s\text{-H}$ bond lengths 0.97 Å and 0.98 Å. This configuration was indeed found to be more stable than the molecular configuration, as shown in Table 5. Note that some tilting of the surface oxygen atoms is observed in this “molecular to dissociative” configuration. This could be a result of the way in which the surface dipole of the {100} surface is eliminated: moving half of the oxygen atoms from the top of the oxygen-terminated surface means that there is little to prevent the remaining oxygen atoms from falling into their place.

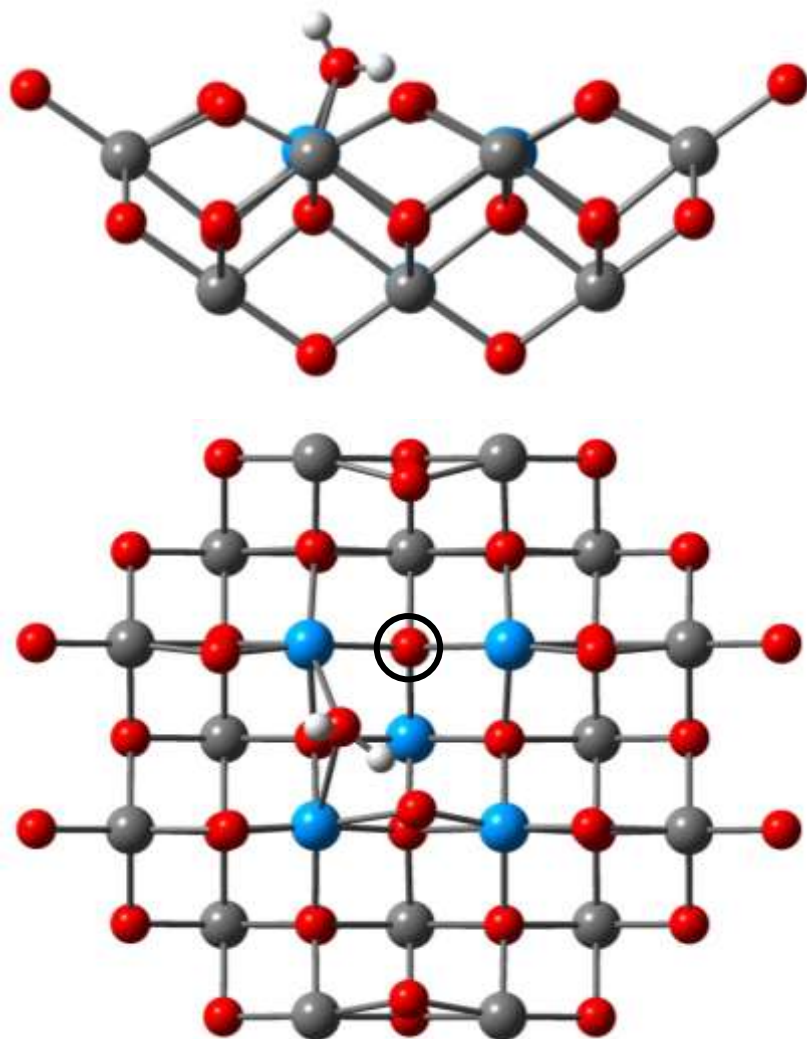


Figure 15 Molecular adsorption of a single water molecule on the {100} surface of a $U_5U_{16}O_{41}$ embedded cluster. Top view shows the cluster in the plane of the surface, while the bottom view is perpendicular to the surface. Hydrogen atoms are shown in white, oxygen atoms in red and uranium atoms in blue and grey. The position of the oxygen vacancy is indicated with a black circle.

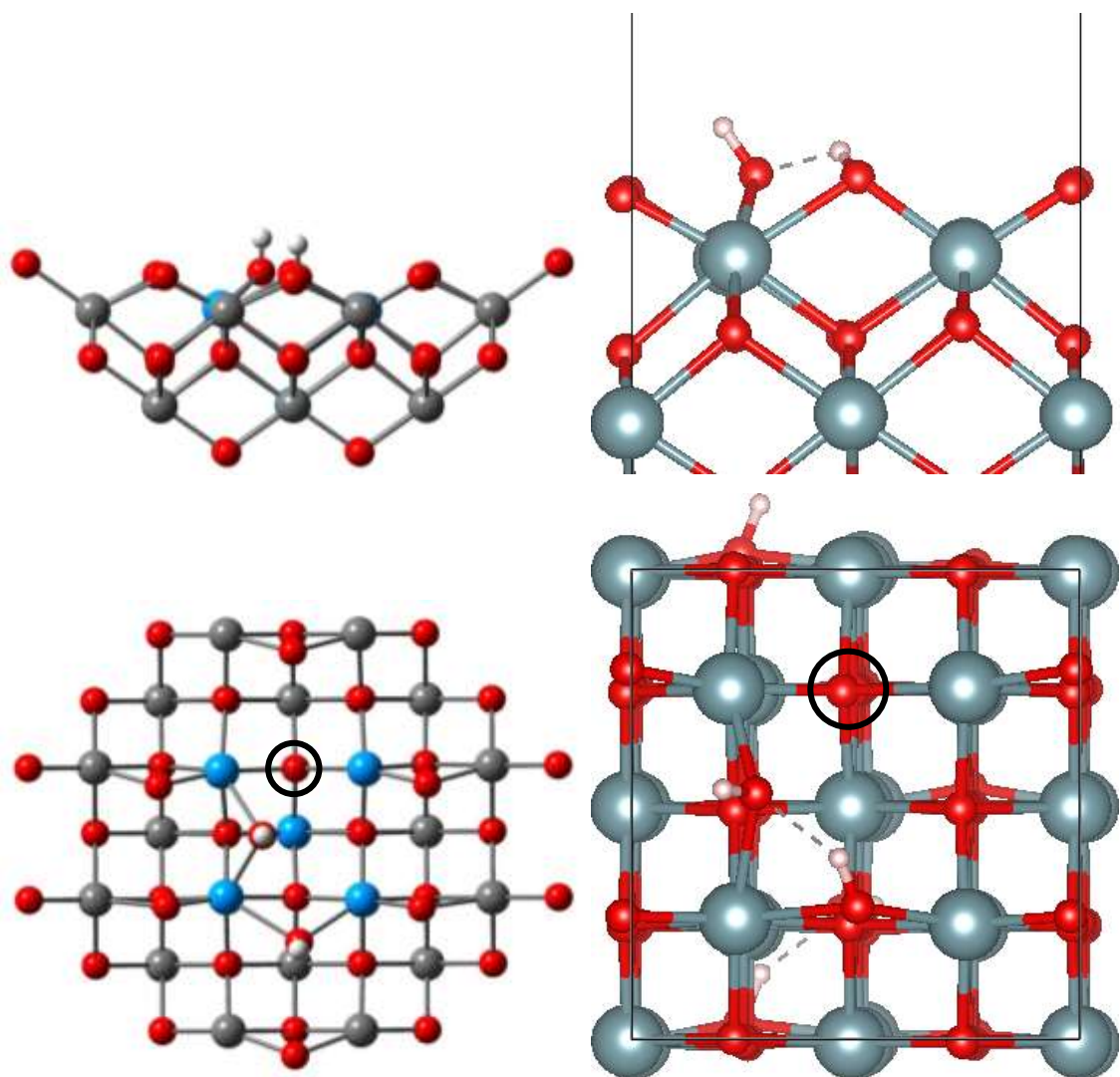


Figure 16 (left) Molecular-to-dissociative adsorption of a single water molecule on the {100} surface of a $U_5U_{16}O_{41}$ embedded cluster. Top view shows the cluster in the plane of the surface, while the bottom view is perpendicular to the surface. Hydrogen atoms are shown in white, oxygen atoms in red and uranium atoms in blue and grey. **(right)** Molecular-to-dissociative adsorption of a single water molecule on the UO_2 {100} slab, near the oxygen vacancy. The top panel shows the side-on view of half the slab and the bottom panel shows the view from above. Hydrogen atoms are shown in white, oxygen atoms in red and actinide atoms in light grey. Dashed lines are hydrogen bonds. The position of the oxygen vacancy is indicated with a black circle.

A second dissociative adsorption was also considered, in which the hydroxyl formed upon dissociation was used to heal the defect site with the remaining hydrogen atom forming a second hydroxyl group on a neighbouring surface oxygen atom. This configuration (also found by Bo *et al.* for reduced NpO_2 ⁵⁶ and Molinari *et al.* for reduced CeO_2 ³³) is depicted in Figure 17.

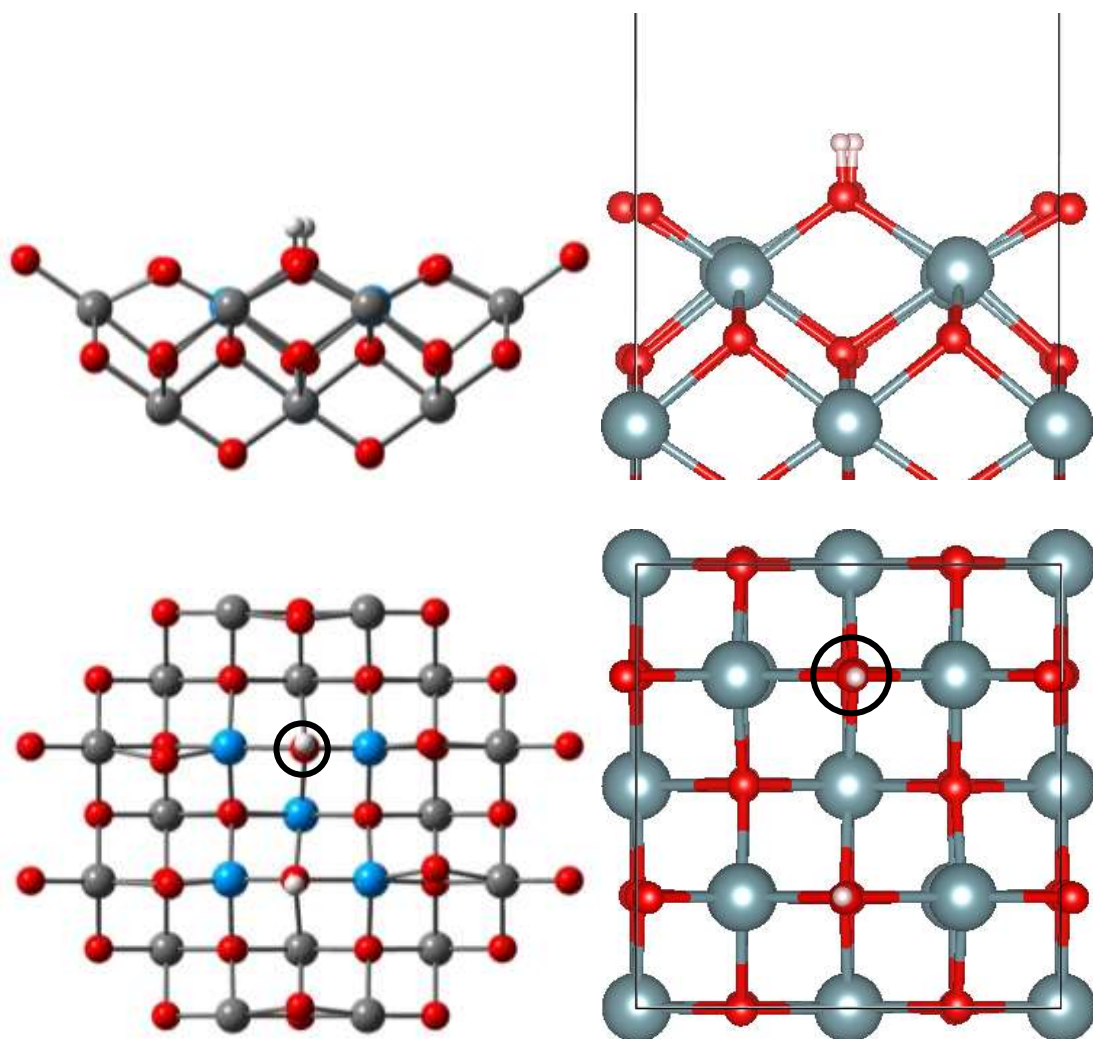


Figure 17 (left) Dissociative adsorption of a single water molecule on the $\{100\}$ surface of a $U_5U_{16}O_{41}$ embedded cluster. Top view shows the cluster in the plane of the surface, while the bottom view is perpendicular to the surface. Hydrogen atoms are shown in white, oxygen atoms in red and uranium atoms in blue and grey. **(right)** Dissociative adsorption of a single water molecule on the UO_2 $\{100\}$ slab, at the oxygen vacancy. The top panel shows the side-on view of half the slab and the bottom panel shows the view from above. The position of the oxygen vacancy is indicated with a black circle.

(ii) Geometries - periodic calculations

As for the other surfaces, a substoichiometric slab where the oxygen vacancy is in the outermost layer was used to investigate water adsorption on the $\{100\}$ surface. Molecular and dissociative adsorption at or near an oxygen vacancy were both investigated. For molecular adsorption a water molecule was placed in the same position as on the stoichiometric surface, and a geometry optimisation was performed. Although introduced molecularly, the water molecule dissociates above the oxygen vacancy, forming two OH-groups; this is the “molecular-to-dissociative” adsorption see in the embedded cluster calculations - the optimized structure is

shown in the right hand part of Figure 16 for UO_2 . The U- O_w distances decrease compared with the stoichiometric case, from 2.61 to 2.36 Å, and the equivalent shortening for PuO_2 is from 2.58 to 2.35 Å. However, this comparison is questionable given that we are comparing a molecular with a dissociative adsorption.

The second type of adsorption, in which we consider dissociation from the start, is shown on the right hand side of Figure 17 for UO_2 . The An- O_sH distances change compared with the stoichiometric case, with the U- O_sH distance increasing from 2.33 to 2.43 Å and the Pu- O_sH distance from 2.29 to 2.38 Å. Here, the changes are similar compared to the {111} surface, and larger compared to the {110} surface.

(iii) Energies

Adsorption energies for each type of adsorption using both methods are given in Table 5. Compared with the stoichiometric surface, the periodic calculations show that for the molecular-to-dissociative case (Dissociative1), adsorption energies increase by 0.65 eV for UO_2 and by 1.47 eV for PuO_2 . However, as these increases are vs intact molecular adsorption on the stoichiometric surface, we will not explore them further. For purely dissociative adsorption (Dissociative2) the effect is similar to the {110} surface, with adsorption energies increasing by 0.88 eV for UO_2 and by 1.06 eV for PuO_2 . That said, the changes in adsorption energy on the {100} surface are more similar to the {111} surface, with dissociative adsorption being strongly preferred for both the reduced {111} and {100} surfaces, whereas on the reduced {110} surface, dissociative adsorption is only slightly increased.

Adsorption Type	Embedded cluster		Periodic	
	UO_2	PuO_2	UO_2	PuO_2
Molecular	-1.76	–	–	–
Dissociative1 ^a	-2.38	–	-1.62	-2.59
Dissociative2 ^b	-3.07	–	-2.43	-2.82

Table 5 Water adsorption energies (eV) on the reduced UO_2 and PuO_2 {100} surfaces. ^aDissociative1 adsorption occurs with the hydroxyl groups are tilted, as shown in Figure 16. ^b Dissociative2 adsorption occurs with the hydroxyl groups vertical, as shown in Figure 17.

The embedded cluster calculations clearly indicate that on the reduced UO_2 {100} surface, dissociative adsorption of water is the most energetically favourable. The

most stable configuration is that in which the dissociated hydroxyl “heals” the vacancy. This trend is also found by our periodic DFT results, with no stable molecular adsorption geometry being located. Although there have been no previous investigations into the adsorption of water onto the reduced {100} surface of UO_2 or PuO_2 , analogous trends have been found by Bo *et al.* and Molinari *et al.* in their work on reduced NpO_2 ⁵⁶ and CeO_2 ³³ surfaces respectively, who also concluded that there was a strong preference for dissociative over molecular adsorption in both of these systems.

Natural population analysis of the substoichiometric UO_2 {100} surface cluster shows that in the case of molecular and molecular-to-dissociative adsorption, the two unpaired electrons left behind by the oxygen vacancy localise on the two uranium atoms directly neighbouring the vacancy (with spin densities of 2.92–3.00 a.u. compared with 2.03–2.19 a.u. on the remaining uranium atoms). For the second type of dissociative adsorption (where the hydroxyl “heals” the vacancy) both electrons also localise, however one of these is now on a uranium atom neighbouring the second surface hydroxyl.

Inclusion of dispersion corrections increases the adsorption energies, in the same way as was found for the {111} and {110} surfaces. For the UO_2 {100} surface dispersion corrections increased the energy by 0.18–0.23 eV (data not shown).

Conclusions

In this contribution, we have for the first time brought together our embedded cluster (PEECM) and periodic boundary condition DFT approaches to study low index surfaces of the actinide dioxides UO_2 and PuO_2 , focusing on the creation of oxygen vacancy defects and the adsorption of water at or near those defects. Both approaches indicate that upon creation of the vacancies, the neighbouring actinide ions relax away from the oxygen vacancy for both the first and second layers, while the surrounding oxygen sub-lattice relaxes towards the vacancy. First layer oxygen vacancies generally have lower formation energies than second layer ones; although the difference on the $\{111\}$ surface is minor, it is more significant on the $\{110\}$ and $\{100\}$ surfaces. As has been seen in other studies of fluorite metal oxide systems, oxygen vacancies are generally easier to produce on the first layer of the $\{110\}$ surface than the $\{111\}$ surface, which is related to the lower coordination number of the actinides on the $\{110\}$ surface than the $\{111\}$. The creation of an oxygen vacancy leaves two electrons behind, reducing the surrounding metal ions. Pu(IV) is much more easily reduced than U(IV), and hence oxygen vacancy formation energies are much (c. 50%) smaller on the PuO_2 surfaces than the UO_2 . Such differences question the use of UO_2 as a surrogate for PuO_2 .

In previous papers, we reported that the energies of molecular and dissociative water adsorption on the stoichiometric $\{111\}$ surface are similar to one another.^{1,2} This situation changes very significantly on the reduced $\{111\}$ surface for, while the energy of molecular adsorption is similar to that found on the stoichiometric surface, that of dissociative adsorption is much larger. These conclusions provide a potential interpretation of previous experimental studies of water adsorption on stoichiometric and substoichiometric UO_2 $\{111\}$.⁵⁴ While water adsorption is reversible on the pristine surface, that on the reduced surface leads to H_2 production, implying dissociative adsorption.

For the stoichiometric $\{110\}$ and $\{100\}$ surfaces, we previously discovered that dissociative adsorption was favoured over molecular. This is also true on the reduced surfaces; indeed, for the reduced $\{100\}$ surface at the PBE+ U level we could not locate molecular adsorption on either UO_2 or PuO_2 , as the water dissociated during geometry optimisation. Thus all three surfaces studied favour dissociative

over molecular water adsorption at oxygen vacancies. Given that such vacancies will be being constantly created by the radioactive decay of the Pu in the storage cans, we conclude that the first monolayer of water on the {111}, {110} and {100} surfaces will be dissociatively adsorbed, with clear implications for the production of H₂ gas. The mechanism for the formation of H₂ following dissociative adsorption will be the subject of future studies from our group.

Acknowledgements

We are grateful to the National Nuclear Laboratory and the EPSRC's M3S Centre for Doctoral Training for studentship funding to JPWW, and to Sellafield Limited and the University of Manchester for a PhD studentship to JC. We thank the EPSRC's "DISTINCTIVE" consortium (<http://www.distictiveconsortium.org>, EP/L014041/1) for funding. We thank the University of Manchester for computing resources via the Computational Shared Facility (CSF) and for access to the "Polaris" cluster at the N8 HPC Centre of Excellence, provided and funded by the N8 consortium and EPSRC (Grant No.EP/K000225/1). The Centre is co-ordinated by the Universities of Leeds and Manchester. We also thank University College London for computing resources via Research Computing's "Legion" cluster (Legion@UCL) "Grace" cluster and associated services, and the "Iridis" facility of the e-Infrastructure South Consortium's Centre for Innovation. We are also grateful to the HEC Materials Chemistry Consortium, which is funded by EPSRC (EP/L000202), for access to ARCHER, the UK's National Supercomputing Service (<http://www.archer.ac.uk>). Finally, we thank Howard Sims and Robin Orr of the National Nuclear Laboratory, and Jeffrey Hobbs and Helen Steele at Sellafield Ltd, for helpful discussions.

References

- (1) Wellington, J. P. W.; Kerridge, A.; Austin, J.; Kaltsoyannis, N. Electronic Structure of Bulk AnO_2 ($\text{An} = \text{U}, \text{Np}, \text{Pu}$) and Water Adsorption on the (111) and (110) Surfaces of UO_2 and PuO_2 from Hybrid Density Functional Theory within the Periodic Electrostatic Embedded Cluster Method. *J. Nucl. Mater.* **2016**, *482* (182), 124–134.
- (2) Tegner, B. E.; Molinari, M.; Kerridge, A.; Parker, S. C.; Kaltsoyannis, N. Water Adsorption on AnO_2 {111}, {110}, and {100} Surfaces ($\text{An} = \text{U}$ and Pu): A Density Functional Theory + U Study. *J. Phys. Chem. C* **2017**, *121* (3), 1675–1682.
- (3) Kresse, G.; Hafner, J. Ab Initio Molecular Dynamics for Liquid Metals. *Phys. Rev. B* **1993**, *47* (1), 558–561.
- (4) Kresse, G.; Hafner, J. Ab Initio Molecular-Dynamics Simulation of the Liquid-Metal-Amorphous-Semiconductor Transition in Germanium. *Phys. Rev. B* **1994**, *49* (20), 14251–14269.
- (5) Kresse, G.; Furthmüller, J. Efficiency of Ab-Initio Total Energy Calculations for Metals and Semiconductors Using a Plane-Wave Basis Set. *Comput. Mater. Sci.* **1996**, *6* (1), 15–50.
- (6) Kresse, G.; Furthmüller, J. Efficient Iterative Schemes for Ab Initio Total-Energy Calculations Using a Plane-Wave Basis Set. *Phys. Rev. B* **1996**, *54* (16), 11169–11186.
- (7) Blöchl, P. E. Projector Augmented-Wave Method. *Phys. Rev. B* **1994**, *50* (24), 17953–17979.
- (8) Kresse, G.; Joubert, D. From Ultrasoft Pseudopotentials to the Projector Augmented-Wave Method. *Phys. Rev. B* **1999**, *59* (3), 1758–1775.
- (9) Monkhorst, H. J.; Pack, J. D. Special Points for Brillouin-Zone Integrations. *Phys. Rev. B* **1976**, *13* (12), 5188–5192.
- (10) Perdew, J. P.; Burke, K.; Ernzerhof, M. Generalized Gradient Approximation Made Simple. *Phys. Rev. Lett.* **1997**, *78* (7), 1396–1396.

- (11) Dudarev, S. L.; Manh, D. N.; Sutton, A. P. Effect of Mott-Hubbard Correlations on the Electronic Structure and Structural Stability of Uranium Dioxide. *Philos. Mag. Part B* **1997**, *75* (5), 613–628.
- (12) Liechtenstein, A. I.; Anisimov, V. I.; Zaanen, J. Density-Functional Theory and Strong Interactions: Orbital Ordering in Mott-Hubbard Insulators. *Phys. Rev. B* **1995**, *52* (8), R5467–R5470.
- (13) Schoenes, J. Optical Properties and Electronic Structure of UO₂. *J. Appl. Phys.* **1978**, *49* (3), 1463–1465.
- (14) McCleskey, T. M.; Bauer, E.; Jia, Q.; Burrell, A. K.; Scott, B. L.; Conradson, S. D.; Mueller, A.; Roy, L.; Wen, X.; Scuseria, G. E.; Martin, J. Optical Band Gap of NpO₂ and PuO₂ from Optical Absorbance of Epitaxial Films. *J. Appl. Phys.* **2013**, *113* (1), 13515.
- (15) Rák, Z.; Ewing, R. C.; Becker, U. Hydroxylation-Induced Surface Stability of AnO₂ (An=U, Np, Pu) from First-Principles. *Surf. Sci.* **2013**, *608*, 180–187.
- (16) Momma, K.; Izumi, F. VESTA 3 for Three-Dimensional Visualization of Crystal, Volumetric and Morphology Data. *J. Appl. Cryst.* **2011**, *44* (6), 1272–1276.
- (17) Ahlrichs, R.; Bär, M.; Häser, M.; Horn, H.; Kölmel, C. Electronic Structure Calculations on Workstation Computers: The Program System Turbomole. *Chem. Phys. Lett.* **1989**, *162* (3), 165–169.
- (18) Perdew, J. P.; Ernzerhof, M.; Burke, K. Rationale for Mixing Exact Exchange with Density Functional Approximations. *J. Chem. Phys.* **1996**, *105*, 9982.
- (19) Schäfer, A.; Horn, H.; Ahlrichs, R. Fully Optimized Contracted Gaussian Basis Sets for Atoms Li to Kr. *J. Chem. Phys.* **1992**, *97* (4), 2571–2577.
- (20) Eichkorn, K.; Weigend, F.; Treutler, O.; Ahlrichs, R. Auxiliary Basis Sets for Main Row Atoms and Transition Metals and Their Use to Approximate Coulomb Potentials. *Theor. Chem. Acc.* **1997**, *97* (1–4), 119–124.
- (21) Moritz, A.; Cao, X.; Dolg, M. Quasirelativistic Energy-Consistent 5f-in-Core Pseudopotentials for Divalent and Tetravalent Actinide Elements. *Theor. Chem. Acc.* **2007**, *118* (5–6), 845–854.

- (22) Weigend, F.; Furche, F.; Ahlrichs, R. Gaussian Basis Sets of Quadruple Zeta Valence Quality for Atoms H-Kr. *J. Chem. Phys.* **2003**, *119* (24), 12753–12762.
- (23) Küchle, W.; Dolg, M.; Stoll, H.; Preuss, H. Energy-Adjusted Pseudopotentials for the Actinides. Parameter Sets and Test Calculations for Thorium and Thorium Monoxide. *J. Chem. Phys.* **1994**, *100* (10), 7535–7542.
- (24) Cao, X.; Dolg, M.; Stoll, H. Valence Basis Sets for Relativistic Energy-Consistent Small-Core Actinide Pseudopotentials. *J. Chem. Phys.* **2003**, *118* (2), 487–496.
- (25) Grimme, S.; Antony, J.; Ehrlich, S.; Krieg, H. A Consistent and Accurate Ab Initio Parametrization of Density Functional Dispersion Correction (DFT-D) for the 94 Elements H-Pu. *J. Chem. Phys.* **2010**, *132*, 154104.
- (26) Burow, A. M.; Sierka, M.; Döbler, J.; Sauer, J. Point Defects in CaF₂ and CeO₂ Investigated by the Periodic Electrostatic Embedded Cluster Method. *J. Chem. Phys.* **2009**, *130* (2009), 174710.
- (27) Ross, R. B.; Gayen, S.; Ermler, W. C. Ab Initio Relativistic Effective Potentials with Spin-orbit Operators. V. Ce through Lu. *J. Chem. Phys.* **1994**, *100* (11), 8145–8155.
- (28) Shannon, R. D. Revised Effective Ionic Radii and Systematic Studies of Interatomic Distances in Halides and Chalcogenides. *Acta Cryst. Sect. A* **1976**, *32* (5), 751–767.
- (29) Jomard, G.; Amadon, B.; Bottin, F.; Torrent, M. Structural, Thermodynamic, and Electronic Properties of Plutonium Oxides from First Principles. *Phys. Rev. B* **2008**, *78* (7), 75125.
- (30) Prodan, I. D.; Scuseria, G. E.; Sordo, J. A.; Kudin, K. N.; Martin, R. L. Lattice Defects and Magnetic Ordering in Plutonium Oxides: A Hybrid Density-Functional-Theory Study of Strongly Correlated Materials. *J. Chem. Phys.* **2005**, *123* (1), 14703.
- (31) Prodan, I. D.; Scuseria, G. E.; Martin, R. L. Assessment of Metageneralized Gradient Approximation and Screened Coulomb Hybrid Density Functionals on Bulk Actinide Oxides. *Phys. Rev. B* **2006**, *73* (4), 45104.

- (32) Bo, T.; Lan, J.-H.; Wang, C.-Z.; Zhao, Y.-L.; He, C.-H.; Zhang, Y.-J.; Chai, Z.-F.; Shi, W.-Q. First-Principles Study of Water Reaction and H₂ Formation on UO₂ (111) and (110) Single Crystal Surfaces. *J. Phys. Chem. C* **2014**, *118* (38), 21935–21944.
- (33) Molinari, M.; Parker, S. C.; Sayle, D. C.; Islam, M. S. Water Adsorption and its Effect on the Stability of Low Index Stoichiometric and Reduced Surfaces of Ceria. *J. Phys. Chem. C* **2012**, *116* (12), 7073–7082.
- (34) Dorado, B.; Jomard, G.; Freyss, M.; Bertolus, M. Stability of Oxygen Point Defects in UO₂ by First-Principles DFT+U Calculations: Occupation Matrix Control and Jahn-Teller Distortion. *Phys. Rev. B* **2010**, *82* (3), 35114.
- (35) Freyss, M.; Petit, T.; Crocombette, J.-P. Point Defects in Uranium Dioxide: Ab Initio Pseudopotential Approach in the Generalized Gradient Approximation. *J. Nucl. Mater.* **2005**, *347* (1–2), 44–51.
- (36) Iwasawa, M.; Chen, Y.; Kaneta, Y.; Ohnuma, T.; Geng, H.-Y.; Kinoshita, M. First-Principles Calculation of Point Defects in Uranium Dioxide. *Mater. Trans.* **2006**, *47* (11), 2651–2657.
- (37) Nerikar, P.; Watanabe, T.; Tulenko, J. S.; Phillpot, S. R.; Sinnott, S. B. Energetics of Intrinsic Point Defects in Uranium Dioxide from Electronic-Structure Calculations. *J. Nucl. Mater.* **2009**, *384* (1), 61–69.
- (38) Freyss, M.; Vergnet, N.; Petit, T. Ab Initio Modeling of the Behavior of Helium and Xenon in Actinide Dioxide Nuclear Fuels. *J. Nucl. Mater.* **2006**, *352* (1–3), 144–150.
- (39) Finazzi, E.; Di Valentin, C.; Pacchioni, G.; Selloni, A. Excess Electron States in Reduced Bulk Anatase TiO₂: Comparison of Standard GGA, GGA+U, and Hybrid DFT Calculations. *J. Chem. Phys.* **2008**, *129* (15), 154113.
- (40) Yang, Z.; Woo, T. K.; Baudin, M.; Hermansson, K. Atomic and Electronic Structure of Unreduced and Reduced CeO₂ Surfaces: A First-Principles Study. *J. Chem. Phys.* **2004**, *120* (16), 7741–7749.
- (41) Ganduglia-Pirovano, M.; Da Silva, J.; Sauer, J. Density-Functional Calculations of the Structure of Near-Surface Oxygen Vacancies and Electron

- Localization on CeO₂(111). *Phys. Rev. Lett.* **2009**, *102* (2), 26101.
- (42) Fabris, S.; Vicario, G.; Balducci, G.; de Gironcoli, S.; Baroni, S. Electronic and Atomistic Structures of Clean and Reduced Ceria Surfaces. *J. Phys. Chem. B* **2005**, *109* (48), 22860–22867.
- (43) Paier, J.; Penschke, C.; Sauer, J. Oxygen Defects and Surface Chemistry of Ceria: Quantum Chemical Studies Compared to Experiment. *Chem. Rev.* **2013**, *113* (6), 3949–3985.
- (44) Ao, B.; Lu, H. First-Principles Energetics of Rare Gases Incorporation into Uranium Dioxide. *Nucl. Instruments Methods Phys. Res. Sect. B* **2016**, *373*, 102–109.
- (45) Ao, B.; Qiu, R.; Lu, H.; Chen, P. First-Principles DFT+U Calculations on the Energetics of Ga in Pu, Pu₂O₃ and PuO₂. *Comput. Mater. Sci.* **2016**, *122*, 263–271.
- (46) Sun, B.; Liu, H.; Song, H.; Zhang, G.; Zheng, H.; Zhao, X.; Zhang, P. First-Principles Study of Surface Properties of PuO₂: Effects of Thickness and O-Vacancy on Surface Stability and Chemical Activity. *J. Nucl. Mater.* **2012**, *426* (1–3), 139–147.
- (47) Nolan, M.; Parker, S. C.; Watson, G. W. The Electronic Structure of Oxygen Vacancy Defects at the Low Index Surfaces of Ceria. *Surf. Sci.* **2005**, *595* (1–3), 223–232.
- (48) Liu, L.-M.; Zhang, C.; Thornton, G.; Michaelides, A. Structure and Dynamics of Liquid Water on Rutile TiO₂ (110). *Phys. Rev. B* **2010**, *82* (16), 161415.
- (49) Wesolowski, D. J.; Sofu, J. O.; Bandura, A. V.; Zhang, Z.; Mamontov, E.; Předota, M.; Kumar, N.; Kubicki, J. D.; Kent, P. R. C.; Vlcek, L.; Machesky, M. L.; Fenter, P. A.; Cummings, P. T.; Anovitz, L. M.; Skelton, A. A.; Rosenqvist, J. Comment on “Structure and Dynamics of Liquid Water on Rutile TiO₂ (110).” *Phys. Rev. B* **2012**, *85* (16), 167401.
- (50) Schaub, R.; Thostrup, P.; Lopez, N.; Lægsgaard, E.; Stensgaard, I.; Nørskov, J. K.; Besenbacher, F. Oxygen Vacancies as Active Sites for Water Dissociation on Rutile TiO₂ (110). *Phys. Rev. Lett.* **2001**, *87* (26), 266104.

- (51) Bikondoa, O.; Pang, C. L.; Ithnin, R.; Murny, C. A.; Onishi, H.; Thornton, G. Direct Visualization of Defect-Mediated Dissociation of Water on TiO₂(110). *Nat. Mater.* **2006**, *5* (3), 189–192.
- (52) Marrocchelli, D.; Yildiz, B. First-Principles Assessment of H₂S and H₂O Reaction Mechanisms and the Subsequent Hydrogen Absorption on the CeO₂ (111) Surface. *J. Phys. Chem. C* **2012**, *116* (3), 2411–2424.
- (53) Xu, H.; Zhang, R. Q.; Tong, S. Y. Interaction of O₂, H₂O, N₂, and O₃ with Stoichiometric and Reduced ZnO (10 $\bar{1}$ 0) surface,. *Phys. Rev. B* **2010**, *82* (15), 155326.
- (54) Senanayake, S. D.; Idriss, H. Water Reactions over Stoichiometric and Reduced UO₂ (111) Single Crystal Surfaces. *Surf. Sci.* **2004**, *563* (1–3), 135–144.
- (55) Senanayake, S. D.; Waterhouse, G. I. N.; Chan, A. S. Y.; Madey, T. E.; Mullins, D. R.; Idriss, H. The Reactions of Water Vapour on the Surfaces of Stoichiometric and Reduced Uranium Dioxide: A High Resolution XPS Study. *Catal. Today* **2007**, *120* (2), 151–157.
- (56) Bo, T.; Lan, J. H.; Zhao, Y. L.; Zhang, Y. J.; He, C. H.; Chai, Z. F.; Shi, W. Q. Surface Properties of NpO₂ and Water Reacting with Stoichiometric and Reduced NpO₂ (111), (110), and (100) Surfaces from Ab Initio Atomistic Thermodynamics. *Surf. Sci.* **2016**, *644*, 153–164.
- (57) Yang, Z.; Wang, Q.; Wei, S.; Ma, D.; Sun, Q. The Effect of Environment on the Reaction of Water on the Ceria (111) Surface: A DFT+U Study. *J. Phys. Chem. C* **2010**, *114* (35), 14891–14899.
- (58) Fronzi, M.; Piccinin, S.; Delley, B.; Traversa, E.; Stampfl, C. Water Adsorption on the Stoichiometric and Reduced CeO₂ (111) Surface: A First-Principles Investigation. *Phys. Chem. Chem. Phys.* **2009**, *11* (40), 9188.
- (59) Watkins, M. B.; Foster, A. S.; Shluger, A. L. Hydrogen Cycle on CeO₂ (111) Surfaces: Density Functional Theory Calculations. *J. Phys. Chem. C* **2007**, *111* (42), 15337–15341.
- (60) Bo, T.; Lan, J.-H.; Zhao, Y.-L.; Zhang, Y.-J.; He, C.-H.; Chai, Z.-F.; Shi, W.-Q.

- First-Principles Study of Water Adsorption and Dissociation on the UO_2 (111), (110) and (100) Surfaces. *J. Nucl. Mater.* **2014**, 454 (1–3), 446–454.
- (61) Zhang, C.; Michaelides, A.; King, D.; Jenkins, S. Oxygen Vacancy Clusters on Ceria: Decisive Role of Cerium F Electrons. *Phys. Rev. B* **2009**, 79 (7), 75433.
- (62) Esch, F.; Fabris, S.; Zhou, L.; Montini, T.; Africh, C.; Fornasiero, P.; Comelli, G.; Rosei, R. Electron Localization Determines Defect Formation on Ceria Substrates. *Science* **2005**, 309 (5735), 752–755.
- (63) Yang, Z.; Yu, X.; Lu, Z.; Li, S.; Hermansson, K. Oxygen Vacancy Pairs on $\text{CeO}_2(110)$: A DFT+U Study. *Phys. Lett. A* **2009**, 373 (31), 2786–2792.
- (64) Haynes, W. M. *CRC Handbook of Chemistry and Physics*, 96th ed.; CRC Press, 2015.

ToC image

